Icarus 319 (2019) 885–908

Contents lists available at ScienceDirect

Icarus

journal homepage: www.elsevier.com/locate/icarus

Hypotheses for the origin of the Hypanis fan-shaped deposit at the edge of the Chryse escarpment, Mars: Is it a delta?

Jacob B. Adler[*,a], James F. Bell III[a], Peter Fawdon[b], Joel Davis[c], Nicholas H. Warner[d], Elliot Sefton-Nash[e], Tanya N. Harrison[a]

[a] School of Earth and Space Exploration, Arizona State University, ISTB4 Room 795, 781 Terrace Mall, Tempe, AZ 85287, USA
[b] School of Physical Sciences, The Open University, Milton Keynes, Buckinghamshire MK7 7EA, UK
[c] Department of Earth Sciences, Natural History Museum, Cromwell Road, Kensington, London SW7 5BD, UK
[d] Department of Geological Sciences, Integrated Science Center, SUNY Geneseo, One College Circle, Geneseo, NY, 14454, USA
[e] European Space Research and Technology Centre (ESTEC), European Space Agency, Keplerlaan 1, Noordwijk 2201 AZ, The Netherlands

ARTICLE INFO

Keywords:
Mars
Mars surface
Geological processes

ABSTRACT

We investigated the origin of the fan-shaped deposit at the end of Hypanis Valles that has previously been proposed as an ExoMars, Mars 2020, and human mission candidate landing site, and found evidence that the landform is an ancient delta. Previous work suggests that the deposit originated from a time of fluvial activity both distinct from and prior to catastrophic outflow, and crater counting placed the deposit's age at ≥ 3.6 Ga. We found over 30 thin sedimentary strata in the proposed delta wall, and from our slope analysis conclude that the fluvial sequence is consistent with a lowering/retreating shoreline. We measured nearly horizontal bedding dip angles ranging from 0° to 2° over long stretches of cliff and bench exposures seen in HiRISE images and HiRISE stereo DTMs. From THEMIS night IR images we determined that the fan-shaped deposit has a low thermal inertia (150–240 $Jm^{-2}K^{-1}s^{-1/2}$) and the surrounding darker-toned units correspond to thermal inertia values as high as 270–390 $Jm^{-2}K^{-1}s^{-1/2}$. We interpret these findings to indicate that the fan-shaped deposit consists mostly of silt-sized and possibly finer grains, and that the extremely low grade and large lateral extent of these beds implies that the depositional environment was calm and relatively long-lived. Our assessment of the geomorphology and composition seems to indicate that the alluvial fan and mudflow hypotheses are less compatible. From our stratigraphic mapping we interpret the order of events which shaped the region. After the Chryse impact, sediment filled the basin, a confined lake or sea formed allowing a large delta to be deposited near its shoreline, the water level receded to the north, darker sedimentary/volcanic units covered the region and capped the light-toned deposit as hydro-volcanic eruptions shaped the interior of Lederberg crater, freeze/thaw cycles and desiccation induced local fracturing, and finally wrinkle ridges associated with rounded cones warped the landscape following trends in degraded crater rims and existing tectonic features. The ancient deltaic deposit we observe today was largely untouched by subsequent catastrophic outflows, and its surface has been only moderately reshaped by over 3 billion years of aeolian erosion.

1. Introduction

The Hypanis fan-shaped deposit in Xanthe Terra (Fig. 1) has been interpreted as a late Noachian aged delta along the dichotomy boundary (Gupta et al., 2015a; Adler et al., 2016; Gupta, 2015b; Hauber et al., 2009; Sefton-Nash et al., 2015; Fawdon et al., 2018a,b) and as a short-lived mudflow or other alluvial feature (Hauber et al., 2009, 2013; Kleinhans et al., 2010). The proposed delta was a candidate landing site for the future Mars 2020 and ExoMars rover missions for several reasons including: it is positioned at the edge of an open basin; could have been an ideal environment for biosignature formation, concentration, and preservation (see Summons et al., 2011; and has accessible exposures of what could be delta bottomset beds. This work addresses the key questions raised by the community about Hypanis: Is the deposit an ancient delta, as opposed to an alluvial fan or mudflow? Was the ancient topography also an open basin, suggesting a potentially large northern sea? And how does Hypanis fit into the regional geologic timeline and history of Mars? Ultimately, too many uncertainties

* Corresponding author.
E-mail addresses: Jacob.B.Adler@asu.edu (J.B. Adler), Jim.Bell@asu.edu (J.F. Bell III), peter.fawdon@open.ac.uk (P. Fawdon), joel.davis@nhm.ac.uk (J. Davis), warner@geneseo.edu (N.H. Warner), e.sefton-nash@cosmos.esa.int (E. Sefton-Nash), tanya.harrison@asu.edu (T.N. Harrison).

https://doi.org/10.1016/j.icarus.2018.05.021
Received 6 March 2018; Received in revised form 20 May 2018; Accepted 23 May 2018
Available online 24 May 2018

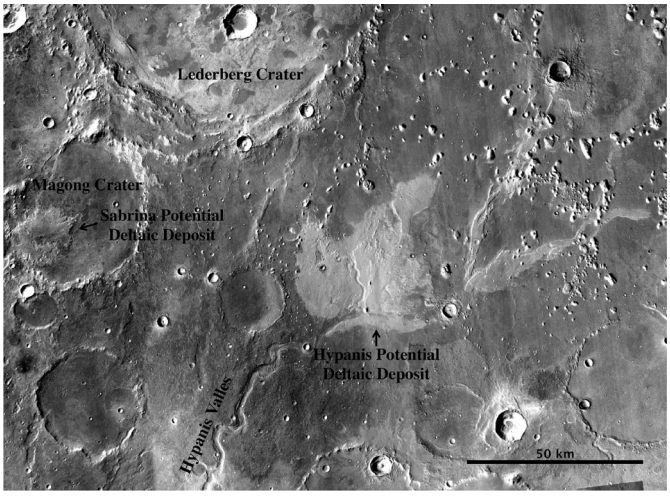

Fig. 1. Mars Reconnaissance Orbiter (MRO) Context Camera (CTX) mosaic of our study region. Hypanis deposit stands out as light-toned in the center. Also marked are Lederberg crater, Magong crater, the Sabrina deposit, and Hypanis Valles.

remained to support the deltaic hypothesis to warrant it being chosen as a finalist in 2016 for the ExoMars mission (Sefton-Nash et al., 2015) or for the Mars 2020 Rover sample caching mission (Gupta et al., 2015a). Questions about the nature and longevity of the aqueous activity were paramount to these landing site discussions. We analyzed NASA Mars Reconnaissance Orbiter (MRO) high-resolution spectral images (Murchie et al., 2007), stereo images (McEwen et al., 2007), and derived digital elevation models, as well as thermal inertia data from the Mars Odyssey Thermal Emission Imaging System (THEMIS) instrument (Christensen et al., 2004) to address the critical unanswered questions raised by the community: Is Hypanis an ancient delta? If so, did it debouch into a large lake or potentially a northern" sea?

While some regions such as Meridiani Planum and Mawrth Vallis have a mineralogic stratigraphy which points to changing geochemical processes indicative of a transition from a warmer and wetter era to a drier one (e.g., Carr and Head, 2010; Bibring et al., 2006; Ehlmann and Edwards, 2014; Carter et al., 2015b; Loizeau et al., 2007), the morphology and size of enigmatic depositional features like those in the Hypanis region are potentially more direct indicators of a wetter past climate (e.g., Malin and Edgett, 1999; Di Achille and Hynek, 2010a; Di Achille and Hynek, 2010b; Rice et al., 2013; Metz, 2009; Adler et al., 2016; Adler et al., 2017; Hauber et al., 2009; Platz et al., 2014). Hypanis is a fan-shaped deposit of light-toned layered stratigraphy which looks strikingly like a delta due to the interpreted presence of an avulsing node and evidence for retreating/prograding motion (Gupta et al., 2015a). The fan-shaped deposit lies along the dichotomy boundary at the Chryse escarpment (Figs. 2 and 3) and is located near several other fan-shaped deposits interpreted to have formed in deltaic environments (e.g., Hauber et al., 2005; Hauber et al., 2009; Hauber et al., 2013; Di Achille and Hynek, 2010b). Hypanis is unique among these nearby potential deltas because it appears to be the largest among them and at the edge of an open basin, not confined to a smaller crater. Fig. 2 shows the distribution of all 53 proposed deltas identified on Mars through 2010 (Di Achille and Hynek, 2010a). This database (Di Achille and Hynek, 2010a) comes from an amalgamation of several publications listing proposed deltas and paleolakes features (including Cabrol and Grinn, 1999, 2001). The authors measured the elevation of the proposed deltaic deposits and valley networks from the Mars Orbiter Laser Altimeter (MOLA) dataset (Smith et al., 2001), and found the elevation of two equipotential surfaces, which could represent two paleoshorelines of a past ocean covering the northern hemisphere of early Mars. Their estimates were compatible with the hypothesized total amount of water predicted by Clifford and Parker (2001) for the Noachian. The Hypanis deposit has an open basin classification, and if the fan was indeed constructed subaqueously, a large northern lake or sea would have been present to account for its extent. The first orbital images of a potential sedimentary deposit at the terminus of Hypanis Valles were sent from Viking Orbiter 1 in 1978 (visual imaging subsystem camera A, image 897*A*25 and camera B, image 650*A*02). In these images a high albedo feature roughly 50 km wide (main lobe) stands out and stretches almost 200 km to the north (Greeley et al., 1977; Crumpler, 1997; Adler et al., 2016; Adler et al., 2017; see supplemental Fig. S1 for first image). Early measurements (Hauber et al., 2005; Kleinhans et al., 2010) of the sediment volume and deposit slopes were not possible until Mars Express High Resolution Stereo Camera (HRSC) imaging (Neukum and Jaumann, 2004). These early studies lead to several interpretations ranging from quick mudflow deposits to large alluvial fans to subaqueous settling of fine sediments (i.e., a delta). But the large pixel scale of these images and their associated terrain models made it impossible to characterize the potential delta in much detail. Thorough evaluation of formation hypotheses is now possible with MRO Context Camera (CTX) (Malin et al., 2007) and High-Resolution Imaging Science Experiment (HiRISE) (McEwen et al., 2007) images of the fan surface; sub-horizontal layering, braided inverted channels, and distal remnant layered islands can now be recognized and studied (Gupta et al., 2015a,b). The deposits at the terminus of Hypanis Valles lie within a region characterized as transition morphology (Tanaka et al., 2014). The upstream catchment to the south consists of early, middle, and late Noachian age units (eNh,mNh,lNh), and the smooth volcanic/flood plains to the north contain large N-S trending wrinkle ridges, defining an age of Hesperian volcanism (early Hesperian transition unit - eHt) (Tanaka et al., 2014; see supplemental

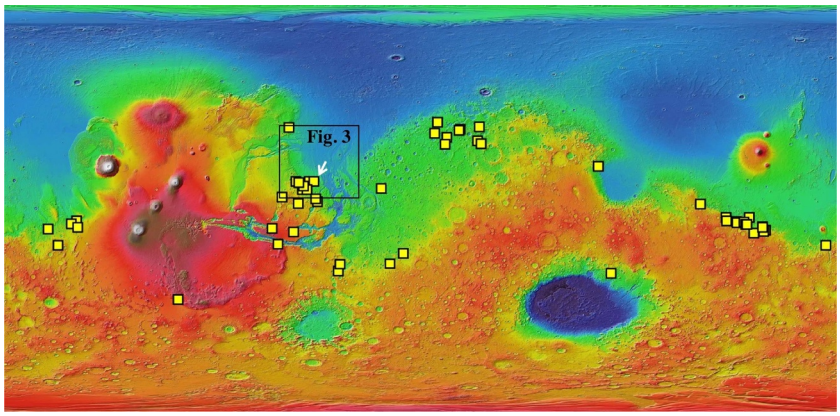

Fig. 2. MOLA colorized elevation map of Mars. Blue is topographic low, red is high. Yellow boxes are locations of deltas mapped by Di Achille and Hynek (2010a,b) and references therein. Hypanis is indicated by the white arrow. NASA/JPL/GSFC. (For interpretation of the references to color in this figure, the reader is referred to the web version of this article.)

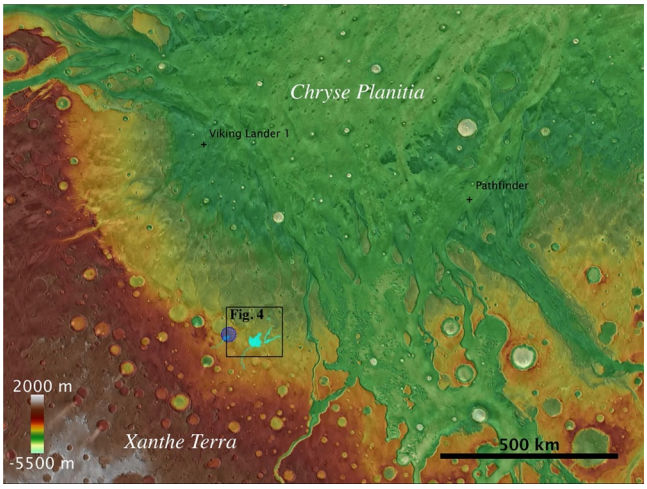

Fig. 3. Shaded topographic map of Chryse basin region. Hypanis fan deposit and neighboring Sabrina deposit are marked in cyan. Sabrina is located in the closed basin of Magong crater, blue, and has been interpreted to be a delta. THEMIS Day IR with MOLA color, NASA/JPL/ASU/GSFC. (For interpretation of the references to color in this figure, the reader is referred to the web version of this article.)

Fig. S2). Farther north in the Chryse plains the Viking 1 lander (1976) and Pathfinder lander (1997) both investigated the Hesperian transition outflow unit (Hto) containing outflow channel fluvial and debris-flow deposits from catastrophic erosion of highland rocks (Tanaka et al., 2014; Nelson and Greeley, 1999; Craddock et al., 1997). The main lobe of the Hypanis fan-shaped deposit appears not to be affected by the major outflow events around 3.2 Ga, and the Hypanis Valles and surrounding upstream terrain similarly seem untouched by the giant flooding of this time (Crumpler, 1997). It is likely, though, that any sediment carried down Hypanis Valles and past the fan deposit has been reworked (as described in Nelson and Greeley, 1999; Crumpler, 1997; Rotto and Tanaka, 1989; Tanaka et al., 2003 with sediment from other catchments into the jumbled outwash flows of the Chryse basin. Recent and ongoing crater chronology studies of the catchment of Hypanis Valles reveal that the downstream fan is at least 3.6 Ga, either early Hesperian or likely late Noachian (Eckes et al., 2016; O'Shea, et al., 2016; Sefton-Nash et al., 2015). This implies that the Hypanis deposit is of a distinct fluvial system older than catastrophic outflow and chaos terrain formation, which occurred around 3.2 Ga (Tanaka, 1997; Fassett and Head, 2008) Further crater counting on the fan deposit itself has proven difficult due to overlying younger aeolian features and extensive erosion. Partly because of such difficulties, the broader regional context and timing of Hypanis remained largely undetermined.

Evidence for volcanism in the region had been observed, including conical and partially collapsed conical features in nearby Lederberg crater proposed to be tuff cones (see Brož and Hauber, 2013), and dark-toned, crater retaining units that appear to display embaying relationships near and upon the proposed Hypanis delta.

Additionally, evidence for volcanism has been documented to the southeast of Hypanis, extending toward the plains surrounding Iani (Harrison, 2012) and Margaritifer Chaos (Salvatore et al., 2016). These volcanics appear to pre-date some of the periods of fluvial activity in the Uzboi-Ladon-Morava valley system, and post-date the formation of chaos terrains, separated by a period of sedimentary deposition within abandoned channels (Salvatore et al., 2016). Similar stratigraphy is observed around Iani, Aurorae, and Hydraotes Chaos, suggesting periods of volcanic activity both before and after chaos formation (Harrison, 2012). Olivine-bearing basaltic units have also been observed up into the Chryse basin (Salvatore et al., 2010). The combined observations in the circum-Chryse region of valley networks, outflow channels, and chaos regions suggest regional-scale fluvial and volcanic modification after the Late Noachian/Early Hesperian (Salvatore et al., 2016; Rodriguez et al., 2007).

The diverse set of geologic units near the Hypanis deposit make the region an exciting study area. While much of the ancient highlands/lowlands dichotomy boundary along the Chryse basin has been erased or reshaped by catastrophic outflow around 3.2 Ga, the Hypanis Valles and deposit region in Xanthe Terra appears to remain untouched by these events. Thus, here we have an example of the largest potential delta on Mars in a location previously hypothesized to be a shoreline of a northern ocean.

2. Methods and data sets

2.1. Hypotheses

We employed a series of tests to assess the likelihood that the Hypanis main lobe is deltaic in origin. To address this hypothesis, we devised a set (Table 1) of tests that could uniquely classify Hypanis as either an ancient delta, mudflow, or alluvial fan. We performed these tests by analyzing MRO Compact Reconnaissance Imaging Spectrometer (CRISM) spectra, THEMIS thermal inertia, HiRISE images, MOLA/CTX/HRSC/HiRISE derived elevation models, and CTX albedo in order to assess the presence of unique signatures belonging to these three kinds of landforms.

In our preliminary analysis, we believed that the wide neck/channel and inverted topography of the secondary lobe could be a sign of changing environmental conditions capping the formation of the underlying fan. We formulated tests (Table 2) to address our hypothesis that the northern lobe was formed by a different process than the main

Table 1
Hypothesis: The Hypanis main lobe is a deltaic deposit.

Process/Landform	Test	Result
Delta	Beds have slope change at topset/foreset	Inconclusive
	Avulsion node migration	Yes
	Basin has evidence of contemporary standing water	Maybe
Mudflow	Larger clasts/boulders incorporated	No
	Levees	No
	Likely source	No
Alluvial fan	Characteristic shape/morphology	Maybe
	Fixed avulsion node	No
	Larger clasts in channels	No

Table 2
Hypothesis: The northern lobe was formed by a different process than the main lobe.

Process/Landform	Test	Result
Rock glacier	Very rocky in HiRISE	No
	High thermal inertia in THEMIS	No
	Moraine at foot	No
	Shape and morphology similar to literature	No
Flow on ice	Topography draped, layers conform	No
Dusty glacier	Glacial morphology, shape	No
	Moraines	No
	No extensive flat bedding	No
Esker	Cross section rounded top	No
	Other regional evidence of glaciation	No
Mudflow	Larger clasts/boulders incorporated	No
	Levees	No
	Likely source	No
Alluvial fan / Delta	Main fan higher in places than northern lobe	Yes

lobe. We utilized these same orbital datasets to assess the likelihood that the northern lobe is an expression of a rock glacier, above-ice deposit, dust/dirt-rich glacier, esker, mudflow, or alluvial fan/delta.

The differences between ancient deltas and alluvial fans on Mars have been ambiguously and inconsistently classified in the literature (see Section 5 of Schon et al., 2012 and discussion in Wood (2006) for detailed summaries of these distinctions). This is mainly due to two limitations: (1) our inability to see the ancient depositional environment and (2) inconsistent definitions or use of geomorphology terms. Here we address these limitations directly.

(1) Mars has likely been devoid of large bodies of surface water for the last 3 Ga. (Carr, 1996; Bell, 2008) During this time, erosional aeolian processes were capable of erasing hundreds of meters of relief (an estimate of 100 nm/yr of erosion during this era is calculated in Kite and Mayer (2017); 300–800 nm/yr vertical rate in Grindrod and Warner (2014), converted from horizontal retreat from landslide-molds, and regional variations likely exist within these estimates). Depositional features from the late Noachian are often affected by not only this severe sandblasting, but also by some combination of cryoturbation, frost and gravity driven mass wasting, chemical alteration, or burial by other sedimentary or volcanic processes.
(2) For the purposes of this paper, a delta is defined as a fan shaped sedimentary deposit formed when fluvial transport reaches a larger body of standing water. Deltaic sediments are deposited subaqueously – by deposition of suspended sediment, building up sedimentary layers. Alluvial fans on Mars often have steeper slopes and consist of larger clasts, cobbles, or boulders, reflecting the higher energy system of mountainous catchments and shorter distance of transport. However, a fan can have any grainsize or gradient depending on conditions. A method for classification based on gradient and grain size alone for alluvial fans and deltaic features on Mars has not yet been developed, and would be insufficient (Blissenbach, 1954; Bull, 1977; Harvey et al., 2005; Catuneanu, 2006; Galloway, 1975; Moore and Howard, 2005; Hardgrove et al., 2009, 2010). (There do exist more detailed distinctions that are common for terrestrial geomorphology (e.g. fan-deltas, megafans, etc.), but that level of complexity was beyond the scope of this work.)

Due to the limitations above (and those summarized in Schon et al., 2012 and Wood, 2006) the most definitive tests for classification of Hypanis as a delta are identification of a dip angle change at the topset/foreset interface (i.e. Lewis and Aharonson, 2006), avulsion node migration, and evidence for a basin which likely held standing water. These qualities are further described below.

2.1.1. Tests for deltaic origin (Table 1)

Table 1 lists the properties discussed in other bodies of literature (Anderson and Anderson, 2010; Bull, 1964) which were both testable and unique to either mudflows, alluvial fans, or deltas. For example, we did not investigate the fan-like shape as that could be indicative of either alluvial fans or deltas. Such a test could not weigh in favor of subaqueous deposition or sporadic sheetwash deposits on land.

A structural architecture found in deltas but not in alluvial fans is that of a bottomset, foreset, and topset bed sequence (Coe, 2003). As a delta forms, nearly flat-lying bottomset beds of fine sediment form at the floor of the lake or sea as lighter particles stay suspended farther out from the shore (Anderson and Anderson, 2010). Steeper slopes (foreset beds) form in succession near the shore. Foreset beds (often sand to pebble sized particles) are coarser grained than bottomset beds (mud sized particles). Classic deltas are topped with nearly flat-lying beds often of mud, sand, and pebbles (topset beds). The angular unconformity (rather, a difference in angles between clinoforms) between foreset and topset beds was identified in several Martian features, including deposits in Jezero crater (Goudge et al., 2017, 2018), and this positive identification is diagnostic of the deltaic environment. We visually inspected anaglyphs and measured the dip angles of beds from HiRISE images draped over HiRISE DTMs of the Hypanis fan-shaped deposit to search for and characterize this interface.

Another testable property of deltas is the migration of the avulsion node, which in alluvial fans stays fixed at the mouth of the system (Ganti et al., 2014). Deposition in deltaic systems is, in general, less energetic and along a lower gradient than alluvial fans, and thus the sweeping back and forth motion migrates. We examined flow direction marks from CTX and HiRISE images under varying illumination conditions to map potential avulsion node locations.

Finally, to help classify a fluvial feature as a delta, we searched for other nearby evidence of a subaqueous environment which could support such a system. We analyzed topography, morphology, and spectra from the region to assess additional supporting evidence of standing water.

Mudflows could be a supported formation mechanism if we see larger clasts or boulders incorporated into the light-toned deposit (Blackwelder, 1928). These short-lived and highly energetic systems can transport large amounts of rock and sediment, whether sourced from melting (jökulhlaups), hot volcanic ash (lahars), avalanches, etc., and these liquefied flows of debris are usually characterized by a poorer grain size sorting than a subaqueous or lacustrine deposit, and are sourced from higher elevation with downslope gradients capable of continuing flow and confinement within channels/canyons to maintain flow depth and speed. HiRISE images and anaglyphs as well as THEMIS thermal inertia data could potentially show larger clasts/boulders and poor grain-size sorting. Visual inspection of CTX images, MOLA global elevation, and our 3D regional mosaic could support this hypothesis if we can identify a likely source. If gradients are lower, mudflows could still travel over a flat expanse by forming levees to channelize the flow (Sharp, 1942; Buffington, 1952). To test that possibility, we view HiRISE images and measure cross-channel transect profiles in HiRISE DEMs to search for mudflow levees.

Specific tests of an alluvial fan hypothesis include identification of a fixed avulsion node, larger clasts and poorer sorting in newer channels, and a characteristic shape (Anderson and Anderson, 2010; Bull, 1964). Bull (1964) defines alluvial fan in a glossary of terms as a stream deposit whose surface forms a segment of a cone that radiates downslope from the point where the stream channel emerges from a mountainous area. We examined flow direction marks from CTX and HiRISE images under varying illumination conditions to map potential avulsion node locations. We examined HiRISE images and anaglyphs as well as THEMIS thermal inertia to investigate larger clasts/boulders and poor grain-size sorting. We viewed HiRISE and CTX mosaicked images to assess the shape and morphology of the light-toned main lobe.

2.1.2. Tests for deltaic origin of distal lobe deposit (Table 2)

During our initial examination, we hypothesized that the distal northern lobe of the Hypanis deposit (fluvial unit B in Fig. 4c) was formed by a different mechanism than the main lobe. We came to this initial conclusion because the lobe seemed simpler in shape and topographically superposed on the main deposit A. The abnormally wide neck of the northern lobe and its inverted relief also made us consider a full range of formation processes. We devised Table 2 in a similar fashion to discriminate between formation mechanisms for the northern lobe with testable observations that are unique to each process. We considered several ice and glacial related processes, as well as mudflow or fluvial origins.

One landform we considered was a rock glacier. If a flow of rocks and ice created the northern lobe shape as ice melted or sublimated, we would expect to see large rocks in HiRISE images and an associated higher thermal inertia derived from THEMIS images. We also might expect to find a moraine near the foot of a rock glacier, and the morphology could be similar to those described in Piatek et al. (2007) and Whalley and Azizi (2003).

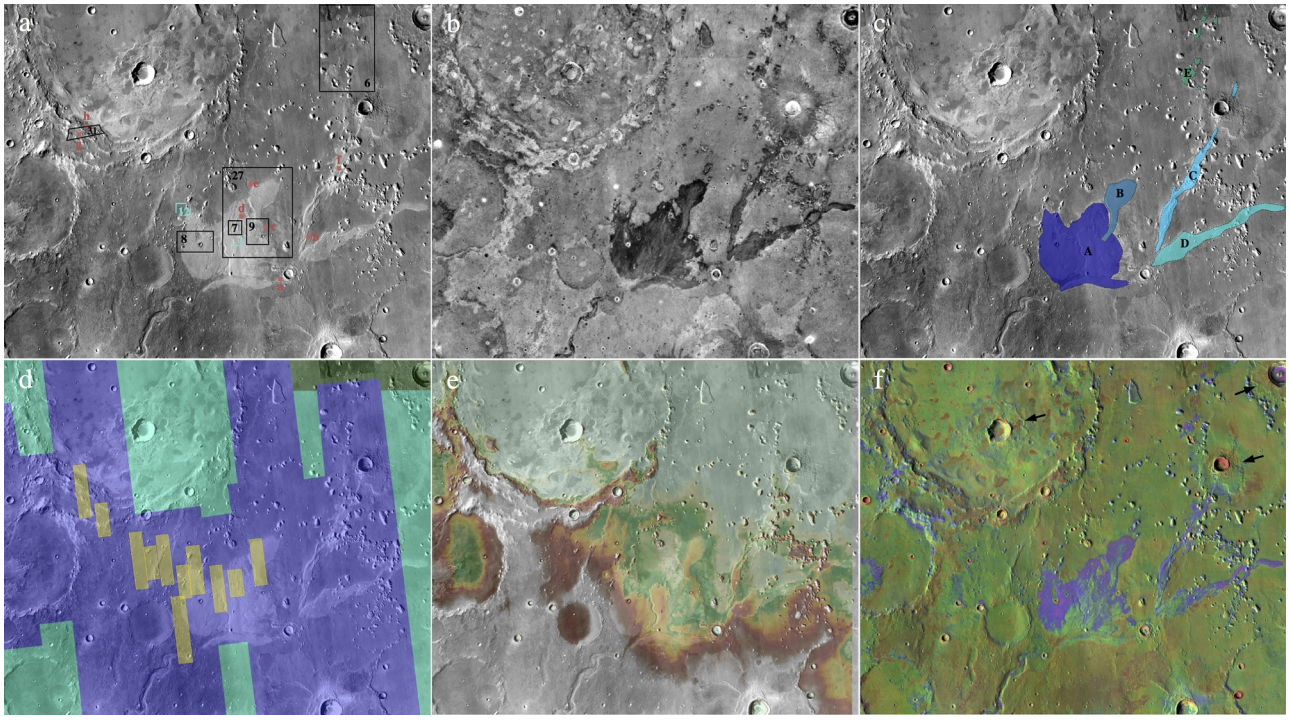

Fig. 4. All images are 175 km wide. (a) CTX mosaic of Hypanis study region showing context for subsequent figures and anaglyphs (black and cyan). Red squares indicate locations of fractures in Figs. 29 and 30. (b) THEMIS Nighttime IR 100m Global Mosaic v14.0 Hill et al. (2014), Edwards (2011) with Northern Hypanis Valles Night IR Mosaic Fergason (2009). Hypanis has a low nighttime temperature. NASA/JPL/ASU. (c) Our proposed fluvial sequence discussed in the text. Main lobe (A) could once have had continuous layered beds spanning to the distal island deposits (E). The cross-cutting relationships we observed are consistent with hypothesized shoreline regression to the north. Flow migrated to the northern lobe (B), then braided inverted channels (C and D) as water retreated. NASA/MSSS/USGS. (d) Coverage map of elevation data. Products were analyzed individually and also merged into one mosaic for visualization and analysis of long profiles. Dark green shows the region where the highest resolution terrain model is MOLA (463 m/pix), teal is HRSC (50, 75 m/pix), blue is CTX stereo (18–24 m/pix), and yellow is HiRISE (1–2 m/pix). Additional HiRISE DTMs are not depicted in the western portion of the image over Sabrina delta, since they were not used in our analysis. Table 1 lists the stereopairs used to generate elevation data. (e) Digital elevation mosaic created from the products listed in Table 1 and outlined in (d). Elevations are displayed from white (-2500 m) to light green (-2800 m). (f) THEMIS Night/Day IR color with CTX mosaic detail. Red colors indicate rocky material, purple represents low thermal inertia fine grain material. Distal island deposits (E) stand out as purple. A few examples of impact craters with slurry ejecta patterns implying past presence of ground ice (Reiss et al., 2006) are marked by black arrows. NASA/JPL/MSSS/ASU. (For interpretation of the references to color in this figure, the reader is referred to the web version of this article.)

We also considered if the northern lobe could be a flow on top of ice, which was later draped onto the main lobe as ice melted or sublimated. If that were the case, we would expect the stratigraphy when viewed in HiRISE images, anaglyphs, and DTMs of the side of the northern lobe or channel to conform to the underlying topography.

We tested if the northern lobe could be a dust or debris covered glacier (Stuurman, 2017). Such a feature might have the characteristic glacial morphology or shape, may have evidence of moraines at its foot, and would likely not consist of extensive horizontal beds.

Since channels C and D (Fig. 4c) appeared inverted, we tested whether the northern lobe and channels C and D could be eskers (see Malin and Edgett, 2003: References and Notes 13 for summary of inverted channels on Mars). A unique test that would support an esker hypothesis is a cross sectional profile of the channel to identify a rounded top. Additional regional evidence supporting glaciation would also bolster this hypothesis.

To test the likelihood that this feature was caused by a mudflow, we utilized the same three tests as for the main lobe. We analyzed HiRISE images and anaglyphs as well as THEMIS thermal inertia data, which could potentially show larger clasts/boulders and poor grain-size sorting; viewed HiRISE images and measured cross-channel transect profiles in HiRISE DEMs to search for mudflow levees; and visually inspected CTX images, MOLA global elevation, and our 3D regional mosaic to try to identify a likely source at higher elevation with downslope gradients capable of continuing flow.

If both the distal northern lobe and the main lobe of Hypanis were part of the same fluvial or alluvial process, then the channel of the distal northern lobe would likely be expressed as a trough within the main lobe, and the distal northern lobe would likely be expressed as a deposit stratigraphically above the main lobe. In this scenario, we might expect to find remnants of the main delta standing higher than the distal northern channel. We measured elevations from our regional DEM mosaic to assess the topography of the main lobe and northern lobe.

2.2. Spectral analyses

We have atmospherically and photometrically corrected CRISM Full-Resolution Targeted (FRT) spectral cubes using the methods described by Seelos et al. (2009) and Seelos et al. (2012) for the CAT (CRISM Analysis Tools) software in ENVI (Environment for Visualizing Images). We then projected the images and created the band parameters recommended by Viviano-Beck et al. (2014), and viewed each of our spectral parameter maps overlayed on either HiRISE (where overlap exists) or CTX images to look for correlations between geomorphic and spectral features. Toggling the CRISM spectral overlays on and off allowed us to validate and speculate whether each parameter map was displaying noise, correlation to atmosphere, surface dust, illumination angle, or other non-relevant phenomena, or whether the spectral parameters are relevant for this study (i.e., correlated to the composition of the geologic units in the catchment or fan). We created ROIs (Regions of Interest) within the CRISM scene using ENVI where we found relevant compositional data, and for each ROI we spectrally averaged the pixels within the ROI and plotted the average spectrum and its standard deviation.

2.3. Thermal inertia analyses

To obtain thermal inertia values we analyzed the atmospherically and photometrically corrected THEMIS numerical images (Fergason et al., 2006) in JMARS (Java for Mission-planning And Remote Sensing; Christensen et al., 2009). Adjacent thermal inertia images can be offset by up to $\sim 200\ Jm^{-2}K^{-1}s^{-1/2}$ due to variations in season and local time of day, but the relative values of geomorphic units within a single image remain roughly constant. We chose THEMIS image I16883014 for our analysis since its footprint spanned the diversity of relevant terrain types. We calculated averaged thermal inertia values of map units from the same pixel columns within that image to avoid bias along the detector.

2.4. Elevation analyses

We constructed 11 HiRISE and 10 CTX digital terrain models (DTMs) from the stereopairs listed in Table 3. Some products were calibrated and formatted with the USGS Integrated Software for Imagers and Spectrometers (ISIS) (i.e. Anderson et al., 2004) and then stereopairs were passed through the Ames Stereo Pipeline (Broxton and Edwards, 2008; Moratto et al., 2010; Beyer, 2015; Shean et al., 2016). We created other products with the software SOCET SET (© BAE Systems). All products were controlled to MOLA shot elevation data. The products range in resolution from 1 to 2 m/pix for HiRISE DTMs and 18–24 m/pix for CTX DTMs. For 3D visualization and drawing of profiles, we used JMARS. For viewing full resolution HiRISE anaglyphs and constructing our anaglyph and DEM mosaics we used ArcGIS. The LayerTools Add-on for ArcMap was used for strike and dip measurements and was provided by Kneissl (see Kneissl et al., 2010).

For profile measurements longer than about 5 km, it was often necessary to sample adjacent terrain models and manually align elevation offsets at the seamlines. We also created a 17 m/pix regional DTM mosaic of our CTX models and filled in the coverage gaps with upsampled HRSC and MOLA (Smith et al., 2001) elevation data. Long slope profiles were derived from this regional mosaic.

Table 3
List of elevation data used in Hypanis region.

Dataset	Resolution (m/pix)	ID (nadir-most)	ID
HiRISE stereopair	1.0	ESP_034249_1920	ESP_034394_1920
	1.0	ESP_021577_1920	ESP_022434_1920
	1.0	ESP_036583_1920	ESP_036517_1920
	1.0	ESP_036161_1920	ESP_036227_1920
	1.0	ESP_037717_1920	ESP_037651_1920
	1.0	ESP_016474_1915	ESP_017186_1915
	1.7	ESP_042003_1920	ESP_041937_1920
	1.0	ESP_039735_1920	ESP_040658_1920
	1.0	ESP_037295_1920	ESP_037005_1920
	2.0	ESP_047805_1925	ESP_049084_1925
	1.0	ESP_034816_1925	ESP_036293_1925
CTX stereopair	17.7	P07_003631_1920	B09_013296_1920
	18.5	B17_016408_1913	G06_020443_1916
	24.0	J03_046104_1918	F05_037783_1918
	17.7	P08_004264_1912	B06_011951_1916
	18.4	G09_021788_1918	G11_022434_1918
	20.2	B17_016474_1915	B19_017186_1915
	24.0	D19_034816_1921	F01_036293_1920
	18.2	P13_006176_1918	F01_036293_1920
	20.2	D07_029845_1921	D07_029990_1921
	20.2	G21_026601_1918	P04_002774_1922
HRSC DA4	75	H2134	
	50	H2145	
	75	H0894	
MOLA Elevation	463	128 ppd Elevation	

Table 4
List of HiRISE images examined in the Hypanis region.

PSP_002141_1915	ESP_036794_1930	ESP_041937_1920
PSP_002919_1915	ESP_036873_1920	ESP_042003_1920
PSP_003842_1935	ESP_037005_1920	ESP_042214_1920
PSP_010250_1915	ESP_037295_1920	ESP_042359_1920
PSP_010817_1920	ESP_037361_1920	ESP_042570_1920
ESP_016474_1915	ESP_037440_1920	ESP_042715_1920
ESP_017186_1915	ESP_037651_1920	ESP_043005_1920
ESP_021577_1920	ESP_037717_1920	ESP_044271_1920
ESP_021788_1920	ESP_037783_1920	ESP_044416_1920
ESP_022434_1920	ESP_037862_1925	ESP_044693_1920
ESP_023001_1925	ESP_038416_1925	ESP_044970_1920
ESP_023278_1925	ESP_038482_1920	ESP_045181_1920
ESP_034249_1920	ESP_039036_1925	ESP_045537_1925
ESP_034394_1920	ESP_039458_1925	ESP_045748_1925
ESP_034816_1925	ESP_039735_1920	ESP_046104_1920
ESP_035528_1920	ESP_040091_1925	ESP_046526_1920
ESP_036161_1920	ESP_040302_1920	ESP_047238_1920
ESP_036227_1920	ESP_040579_1920	ESP_047805_1925
ESP_036293_1925	ESP_040658_1920	ESP_047884_1925
ESP_036517_1920	ESP_041014_1920	ESP_048807_1920
ESP_036583_1920	ESP_041436_1920	ESP_049084_1925
ESP_036728_1925	ESP_041858_1920	

2.5. Albedo analyses

We identified CTX images that looked atmospherically clear, and calibrated and corrected the images in ISIS according to the methods in Bell et al., (2013) and Anderson and Bell (2010). We divided by the cosine of the incidence angle to obtain estimated Lambert albedo images, map projected them, and uploaded them to JMARS.

2.6. Visual analysis

We examined a total of 65 HiRISE observations acquired between years 2007–2017. These images spanned roughly from 11.0° to 13.5° N 313.5°–316.5° E, and helped inform our characterization of the morphology and stratigraphy of the region. Images had a resolution of either 25 or 50 cm/pix. We examined both the color image and larger red band image for each observation listed in Table 4.

3. Results

3.1. General observations

3.1.1. Visual

Upon initial examination of the fan-shaped deposit in CTX and HiRISE images, we divided the light-toned deposit into 5 units. Fig. 4c shows the locations of these units: main lobe (A), a smaller lobe to the north (B), two braided and inverted features (C and D), and small patches further down-slope (E). CTX images (Fig. 5) show paleoflow direction (see Fawdon et al., 2018b for paleoflow timeline interpretation). Lobes A and B are fan shaped, and consist of a build up of multiple flow directions, therefore we marked three potential avulsion node locations (Fig. 5, white arrows). Inverted channels C and D are braided and maintain a NE and ENE heading respectively. Following the paleoflow lineations on their surface, both channel systems appear to source from the same avulsion location which is hidden by a younger superimposed impact crater near the location where channel D crosscuts channel C.

The location of distal light-toned low thermal inertia deposits is shown as E in Fig. 4c, and is more easily seen in Figs. 4b, f, and 6. All

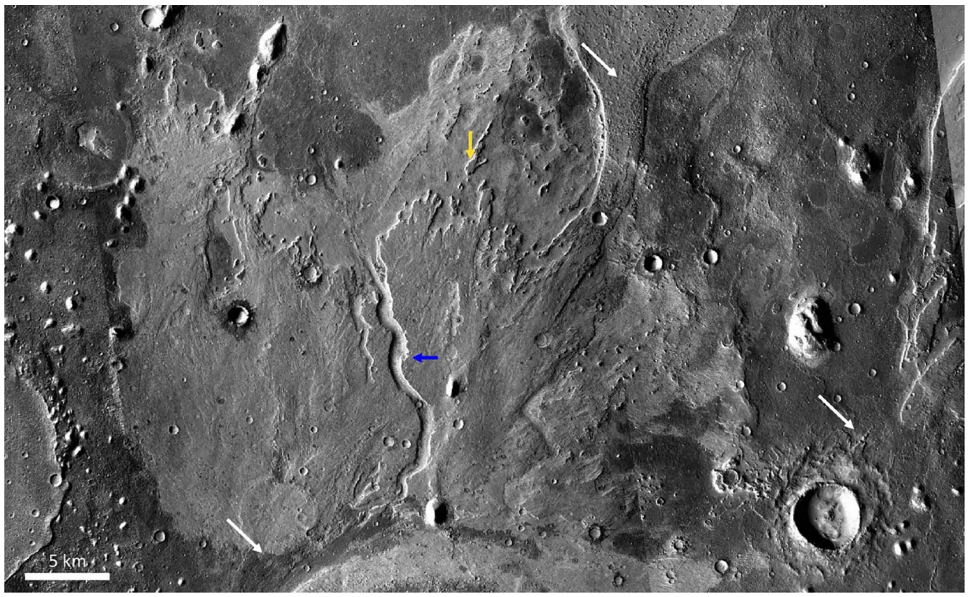

Fig. 5. This CTX mosaic shows paleoflow directions within the light-toned layered deposit and the darker floor unit surrounding it. Three avulsion nodes described in the text are indicated with white arrows. A younger channel (blue arrow) cuts into the main fan deposit and perhaps represents a later reactivation of flow at Hypanis Valles. The view direction of Fig. 22 is indicated by the gold arrow. Layered beds are exposed as cliffs and buttes along the northern perimeter of the main lobe, and these exposures could preserve the stratigraphic depositional history. We examined these locations for evidence of a slope change indicating a transition from foreset to topset beds, and measured the dip angle of beds using Layer Tools. CTX Mosaic: NASA/JPL/MSSS/ASU. (For interpretation of the references to color in this figure, the reader is referred to the web version of this article.)

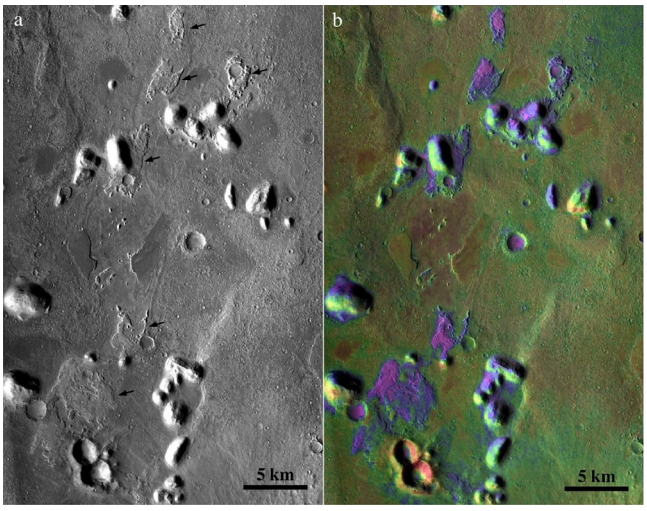

Fig. 6. (a) Distal deposits (black arrows) are found up to 130 km from the apex of the main Hypanis deposit. (b) These remnant islands match the low thermal inertia (purple) of the main fan. The nearest and largest of the distal deposits and is ~ 8 km long. It sits 50 km beyond the current extent of the main lobe (A) and northern lobe (B). Its average albedo was 0.21 and its thermal inertia between 150–200 $Jm^{-2}K^{-1}s^{-1/2}$, which matches the values for the rest of the deposit reported in Table 5. Its topography is raised compared to its surroundings. CTX Mosaic, with color from THEMIS Night/Day IR. Red corresponds to rocky surfaces, and purple corresponds to fine grains. NASA/JPL/MSSS/USGS/ASU. (For interpretation of the references to color in this figure, the reader is referred to the web version of this article.)

five of the fluvial units appear to have similar geology and morphology (we classify the entire fan deposit as belonging to just one facies unit). The units are approximately flat-topped, with subdued topography on their surfaces, and roughly half of the surface is covered by light-toned aeolian bedforms. The fan surface unit is

Table 5
Properties of geomorphic units.

	Geomorphic Unit	Elevation (m)	Albedo	Thermal Inertia ($Jm^{-2}K^{-1}s^{-1/2}$)
1	Hypanis Fan Low TI Unit	−2638 to −2561	0.20–0.21	150–170
2	Hypanis Fan Unit	−2638 to −2561	0.20–0.21	150–240
3	Noachian Highlands	−2290 to −2258	0.18–0.20	190–270
4	Lederberg Low TI	−2820 to −2785	0.20–0.21	230–340
5	Lederberg High TI	−2855 to −2846	0.20–0.21	270–390

dominated by a smooth/soft morphology; lower gradient areas as well as some cliff slopes appear to gently blur the landscape. Many small craters ranging from 0.5 to 10 m in diameter have retained their simple bowl shape (Fig. 7). The smooth light morphology of the deposits surface is contrasted with that of several darker deposits. Fig. 8 shows darker material as ejecta from a crater which punched through the light-toned deposit. This example shows that a darker unit underlies the Hypanis deposit. In other locations, patches of darker deposits overlie the Hypanis deposit (Fig. 9).

3.1.2. Topography

We found that the main lobe and northern lobes were up to 60–100 m thick in some parts. We also found that the light-toned layers were deposited in an open ended (at least at present) bowl shaped depression along the Chryse basin rim, and that rounded buttes stand higher than the layered deposit. In some regions, wrinkle ridges can offset topography by ~ 80 m. We also note that the eastern region of the main lobe is much lower than the western or northern regions, and there exists a 50 m relief escarpment trending N-S in the center of the main lobe (Figs. 10 and 11).

The five light-toned Hypanis fluvial units discussed above are surrounded by darker floor units. We found it helpful to view HiRISE anaglyphs (Figs. 12–19) to investigate the relationship between the Hypanis layers and dark material. In several cases, we found the

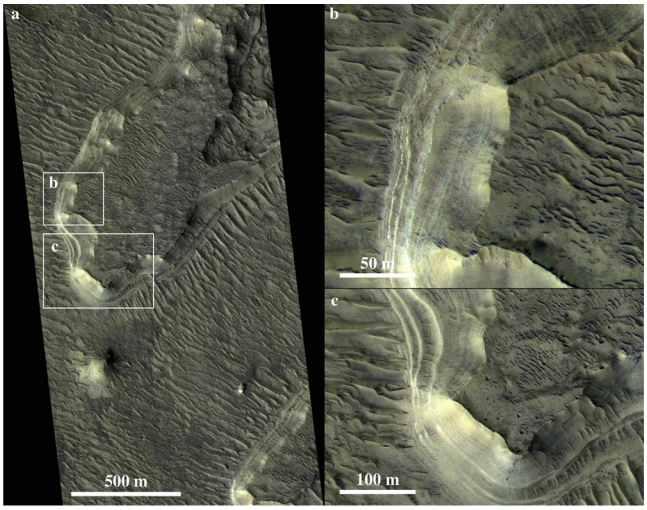

Fig. 7. HiRISE ESP_021577_1920 (a) layered cliffs mark the northern edge of the fan deposit. (b) Boulders can be seen eroding out from the cliff layers. If these meter-sized boulders are clastic that would represent a very energetic transport mechanism which contradicts low gradient of the layers. (c) The soft morphology on the fans surface is dotted with small circular impact craters several meters in width. Where not exposed, the soft unit is covered by transverse aeolian dunes.

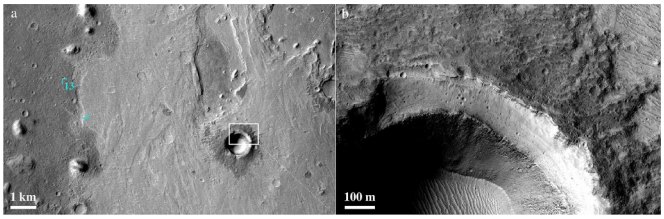

Fig. 8. (a) An impact crater (center right) exposes darker material from underneath (stratigraphically below) the Hypanis light-toned deposit. The location of anaglyph Fig. 13 is noted (cyan) where a different instance of dark material lies stratigraphically above the west flank of Hypanis. CTX: B17_016474_1915. NASA/JPL/MSSS. (b) The ejecta blanket is dark and retains small craters, suggesting volcanic plains lie beneath the Hypanis deposit. HiRISE: ESP_036161_1920. NASA/MSSS/UA.

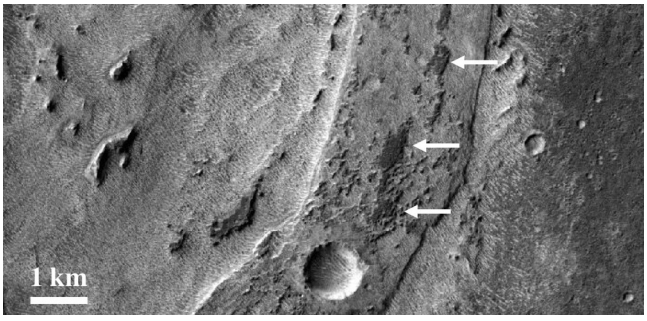

Fig. 9. Inverted channel leading to northern lobe. The channel seems abnormally wide, and has a 50 m scarp along its width. Arrows point to dark patches on the surface which we interpret to be remnants of a volcanic plain covering the layered deposit. CTX Mosaic, NASA/JPL/MSSS/USGS.

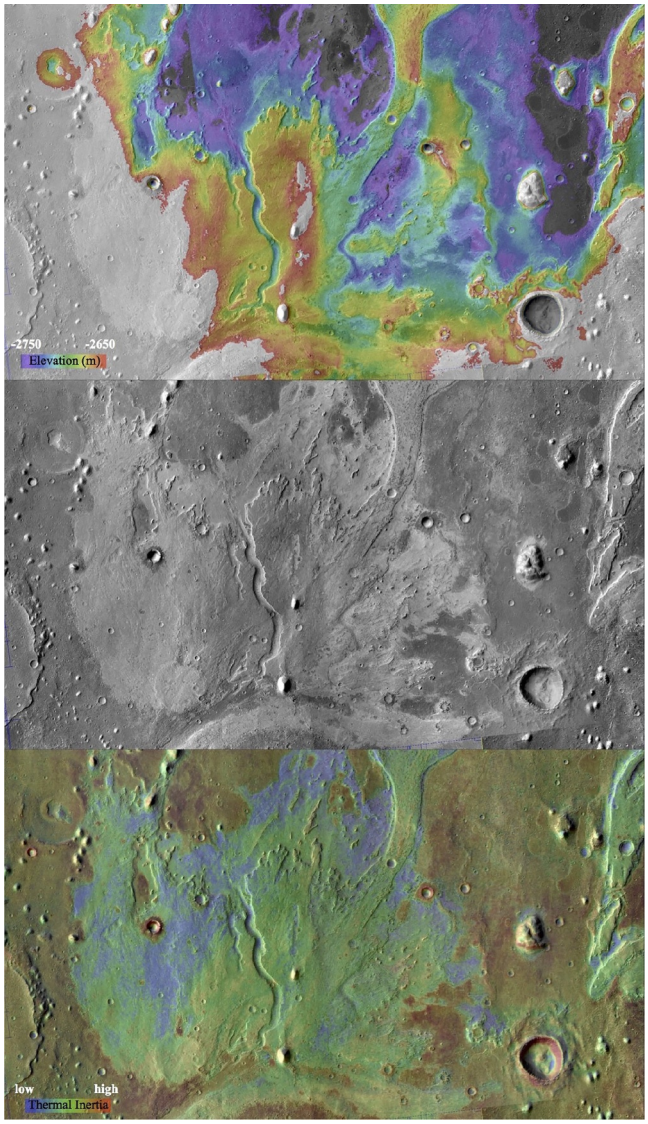

Fig. 10. Three of the datasets used in our study (elevation, albedo, and thermal inertia) show variation within and around the main lobe. Our digital elevation mosaic shows over 100 m of relief in the main lobe from the apex to the deposit front. There are also two notable escarpments of over 50 m in relief: a N-S trending feature in the center of the main lobe and an E-W trending hump along the northern lobe channel. The bottom image is a stretched and colorized THEMIS Night/Day mosaic, used here as a proxy for thermal inertia. The darker units surrounding Hypanis in the center image (CTX mosaic) have a higher thermal inertia, and there is some variation in thermal inertia within the Hypanis deposit, with lower values generally along the flanks. Each image is 60 km wide. (For interpretation of the references to color in this figure, the reader is referred to the web version of this article.)

contact between these two units was topographically expressed as a moat (Fig. 13). We also noted that in some regions the darker floor unit appeared to consist of multiple flow-like morphologies and contained wrinkle ridges not present in the layered deposit. In some locations layered light toned mesas were capped with dark material

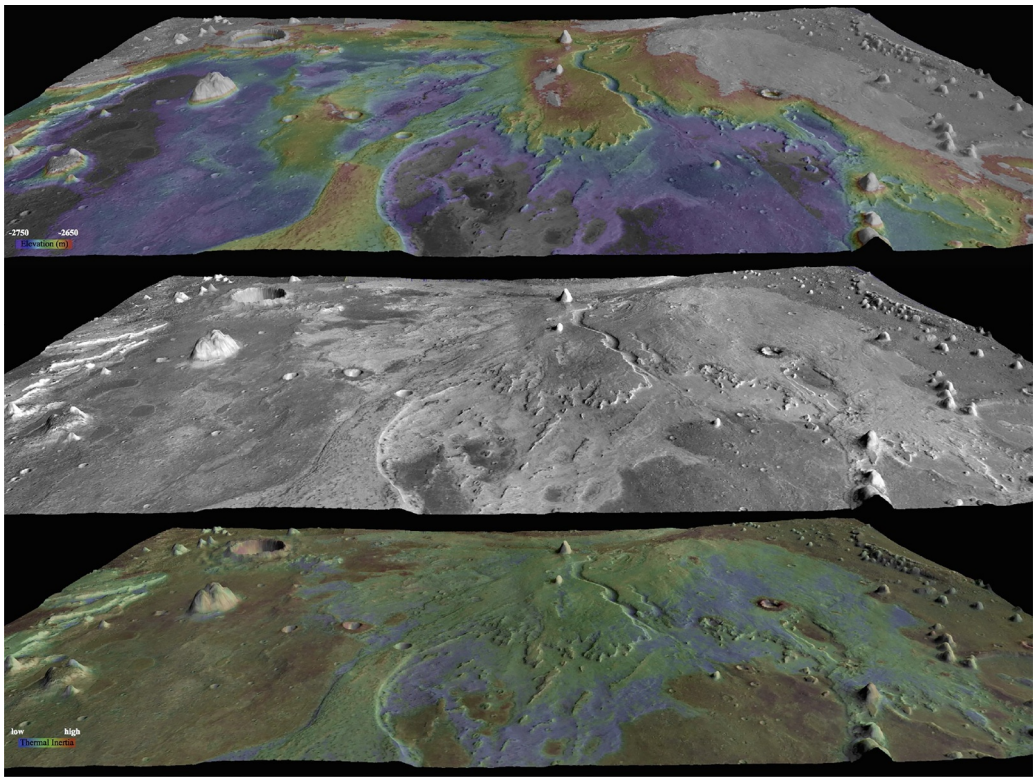

Fig. 11. The three images of Fig. 10 are each draped over our digital elevation model mosaic. View is looking south towards the Chryse escarpment and apex of the Hypanis deposit. The rounded buttes which dot the region have a much greater relief and reach a higher elevation than any of remnant of the Hypanis light-toned deposit. Images are 60 km wide. (For interpretation of the references to color in this figure, the reader is referred to the web version of this article.)

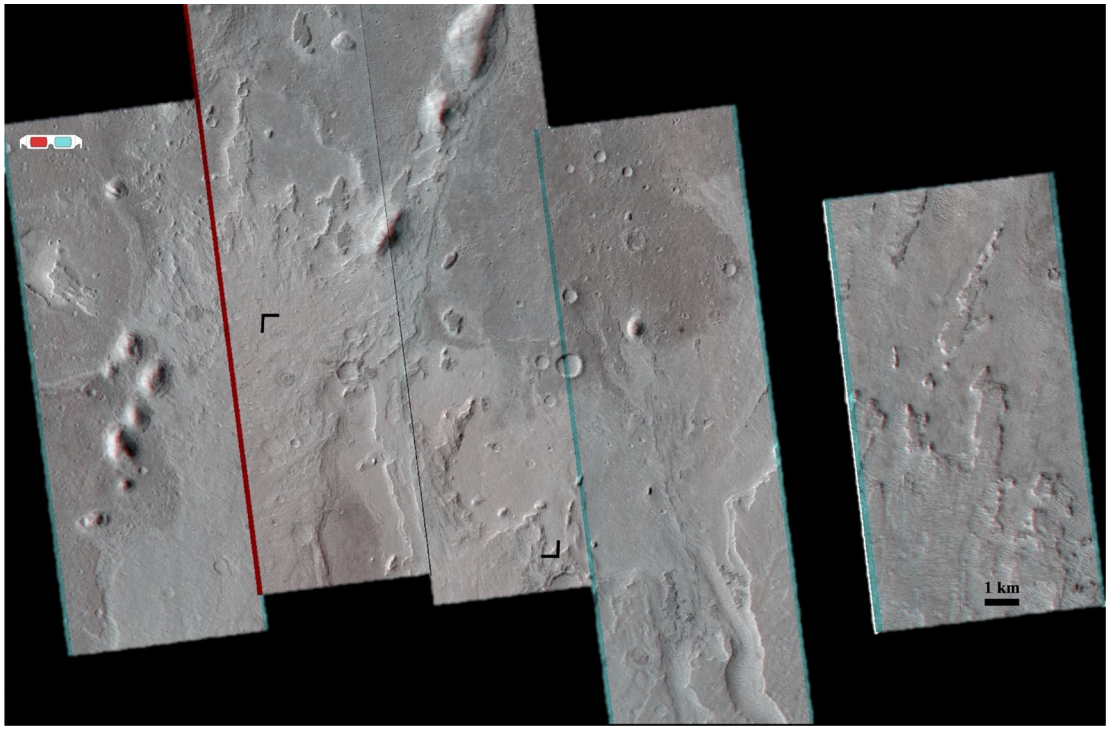

Fig. 12. All figures with the red/blue glasses symbol are HiRISE anaglyphs requiring these glasses to view in 3D. We viewed HiRISE anaglyphs to search the large region for key contacts and stratigraphic information. This image is a mosaic of 5 HiRISE stereopair anaglyphs of the North and West perimeter of the Hypanis main lobe. The largest relief features are the cliffs along the perimeter of the main lobe and the rounded mounds, which appear on both the Hypanis deposit and the darker floor units. The location of Fig. 14 has two corners marked. Additionally, a 1 km wide pit at the westernmost border of the mosaic is also one of the proposed locations for a habitation site mentioned at NASAs Human Landing Site Workshop in October 2015. See Gupta et al. (2015a,b) for more information about potential shelter, resources, water extraction, and science investigations at this candidate site. HiRISE Anaglyph, NASA/JPL/UA.

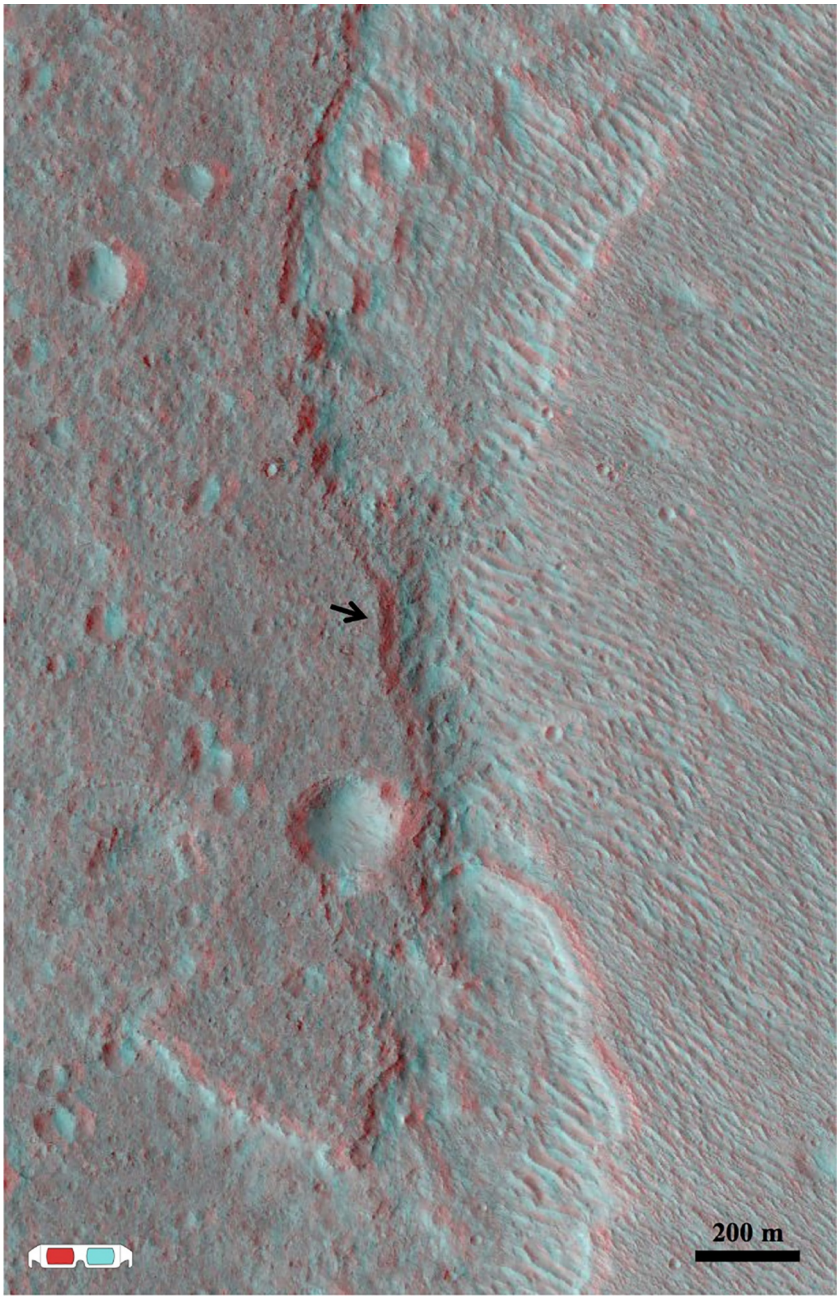

Fig. 13. This figure shows that the contact between the light-toned layered fan-shaped Hypanis deposit (right) and the darker cratered terrain (left) appears to be an onlapping or embaying relationship. A moat separates the two units, and the darker material has a raised ridge (black arrow) along the western edge of the moat, suggesting the darker unit deflated after its emplacement. This location suggests the darker units to the west are younger than the fan deposit. NASA/JPL/UA.

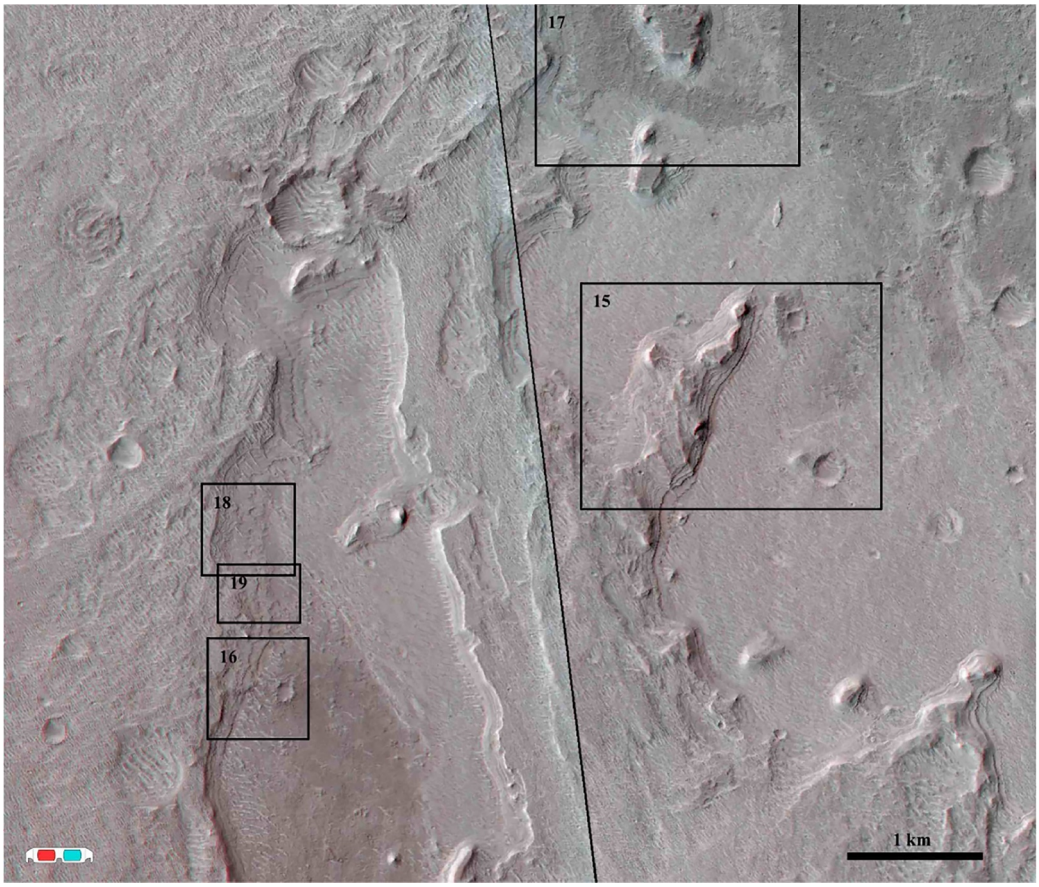

Fig. 14. Context for Figs. 15–19. HiRISE Anaglyph, NASA/JPL/UA.

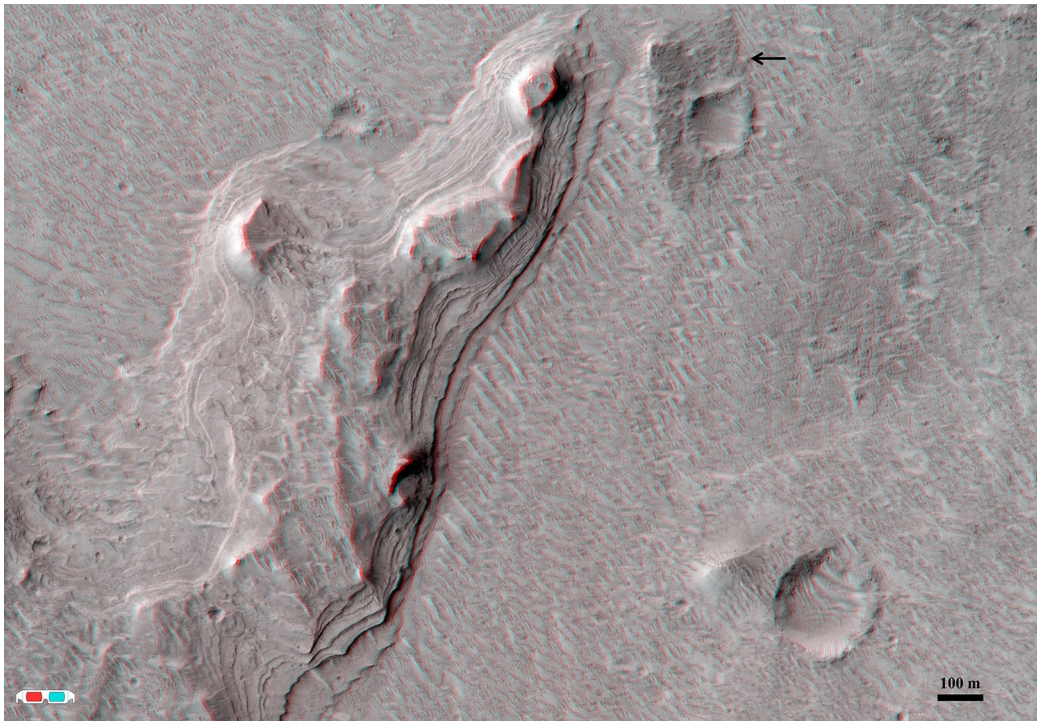

Fig. 15. Cliffs and benches along the northern diffuse border of the main lobe appear flat and laterally continuous. A darker unit near the top of the image (black arrow) appears to slope upward toward the layered beds to its west. This could indicate where the darker unit flowed onto the layered slopes at a time when the fan unit was larger. HiRISE Anaglyph, NASA/JPL/UA.

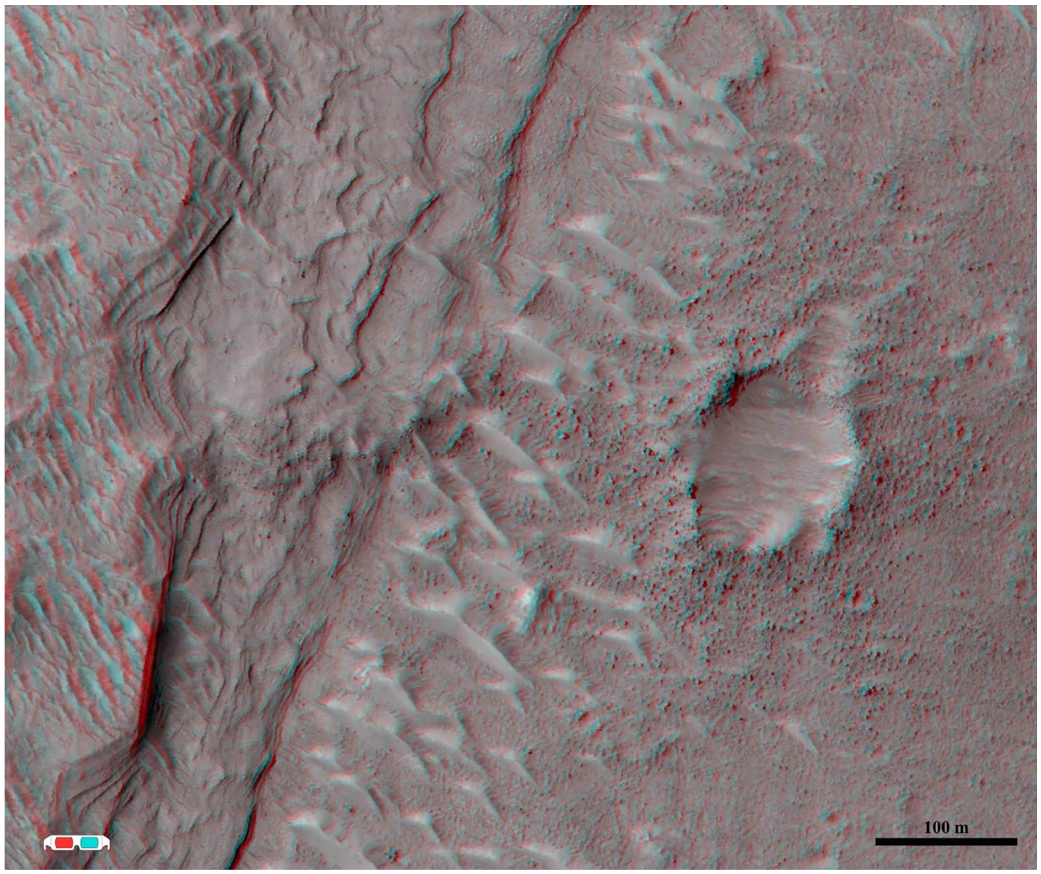

Fig. 16. An impact crater in the floor unit at the base of the cliffs leaves behind an ejecta blanket which has eroded in a different manner than the layered deposit. The ejecta blanket in the floor unit appears to have eroded in place into darker boulders. This contrasts with the fan unit which appears to erode into smaller clasts, possibly contributing to the bedforms which cover the deposit. The bottom-most layers of the Hypanis main lobe contain larger clasts or lighter toned boulders. HiRISE Anaglyph, NASA/JPL/UA.

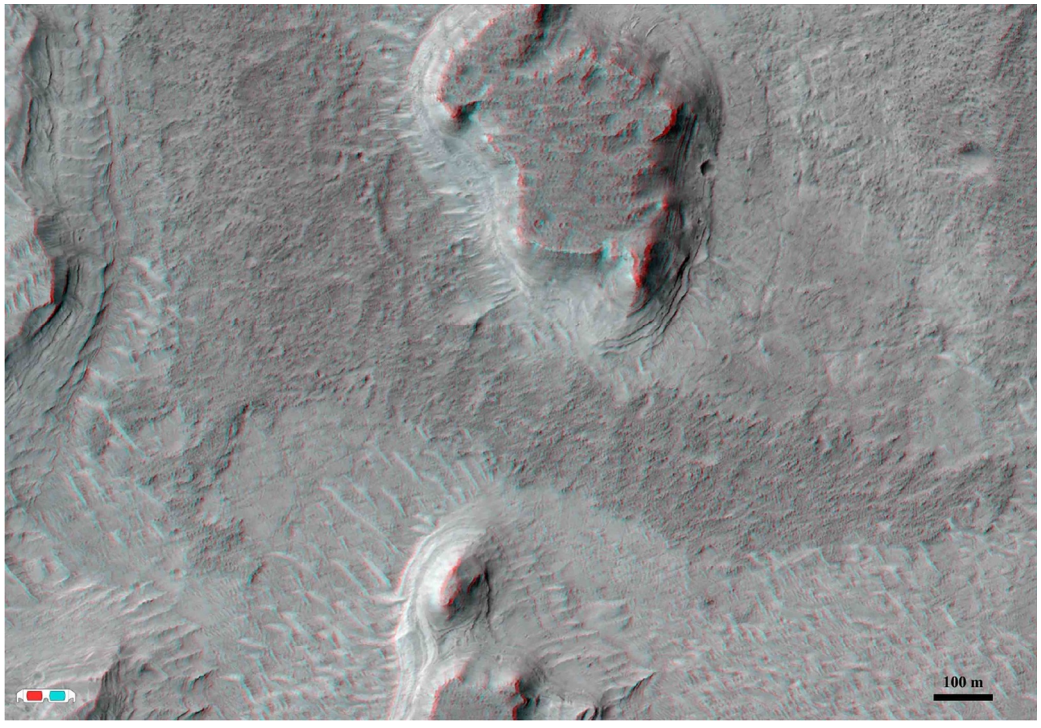

Fig. 17. A mesa (top center) is capped with a darker and more cratered material. This suggests that the cap rock was more extensive, perhaps covering much more or all of the fan shaped deposit. It is also possible that this capping unit helped preserve the underlying layered deposit. In addition to the dark floor unit, there is a second flat-lying fractured floor unit which is more light toned and is situated as an apron of the fan layers. HiRISE Anaglyph, NASA/JPL/UA.

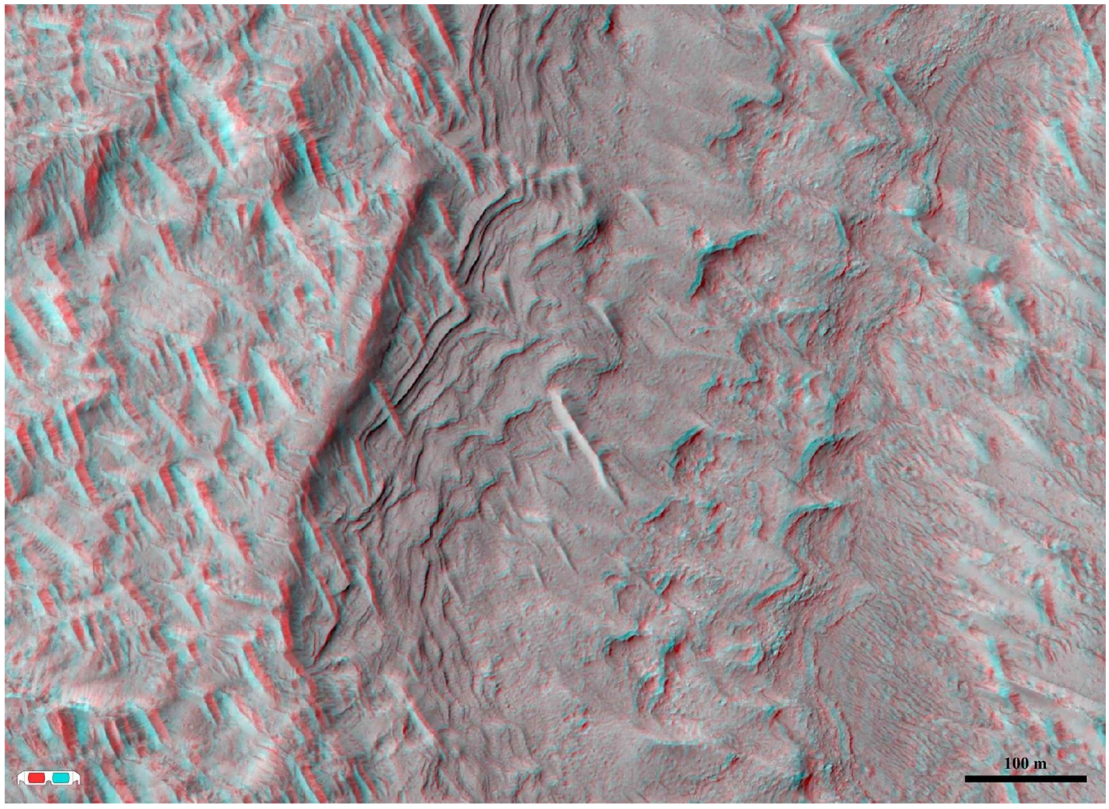

Fig. 18. Layers exposed in the fan-shaped deposit have some variations in textures within the section. The lowest layers identified (right) contain clasts as large as 1–3 m in size. However, no boulders are seen as talus beneath these lower cliff, which raises the question of whether these are not a conglomerate of rocks and boulders eroding out of a matrix, but rather beds of a more uniform and smaller clast size which break into chunks when exposed. The majority of the exposed fan deposit beds in the region are stratigraphically above (left) these rockier or chunkier beds, and no clasts can be observed at HiRISE resolution. On top of the Hypanis layers are Aeolian bedforms. HiRISE Anaglyph, NASA/JPL/UA.

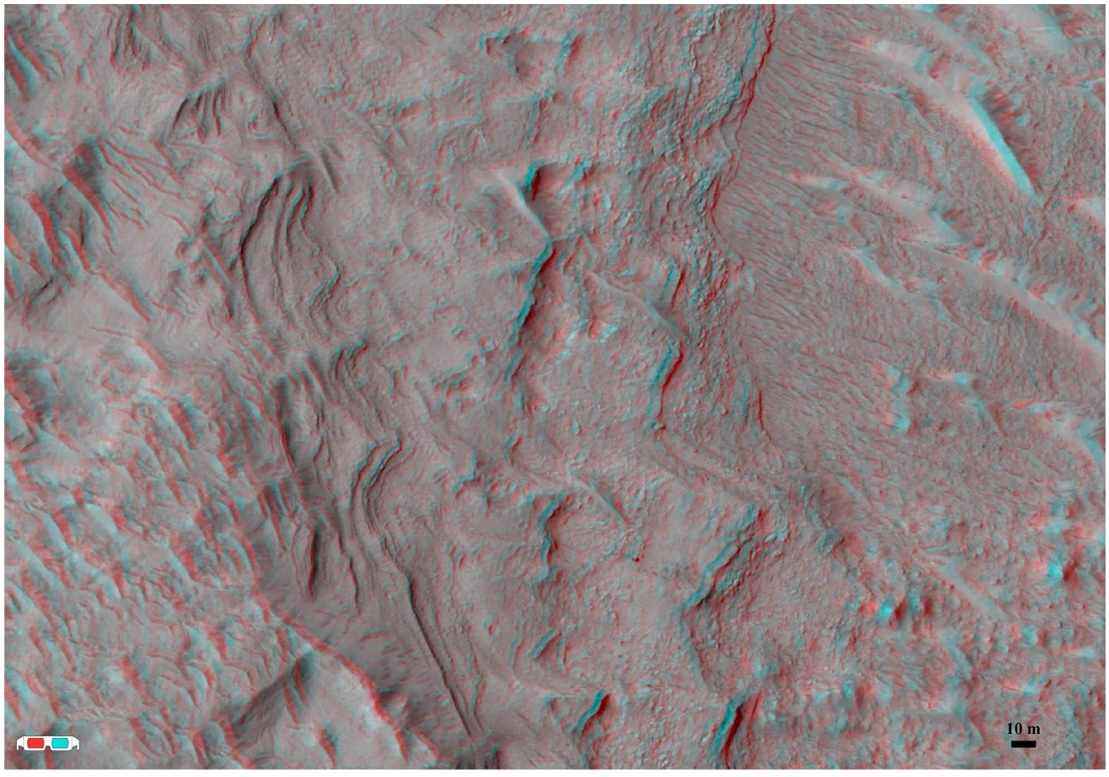

Fig. 19. A closer view of cliff and bench strata near Fig. 18. HiRISE Anaglyph, NASA/JPL/UA.

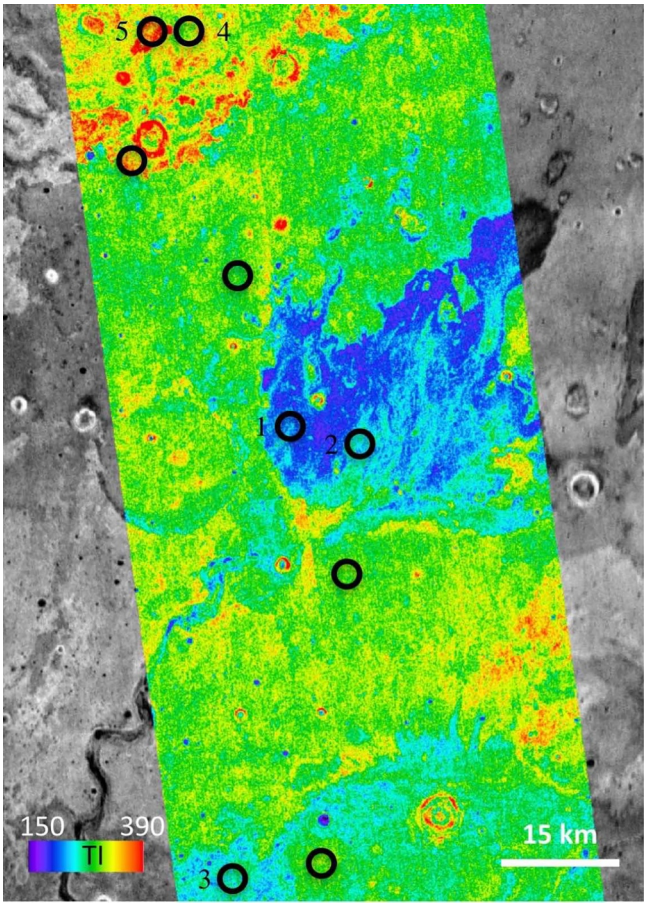

Fig. 20. Thermal inertia from two overlapping THEMIS images I05975009 and I16883014 (values offset to color match other image). Units of thermal inertia are in $Jm^{-2}K^{-1}s^{-1/2}$ and stretched from purple (fine loose grains) to red (rocky). We obtained numerical values by processing THEMIS image I16883014. The thermal inertias of five regions (an average of pixel values within black circular map samples) are listed in Table 5. (For interpretation of the references to color in this figure, the reader is referred to the web version of this article.)

(Fig. 17). The terminus or front of the main lobe is not continuous. Buttes and mesas with steep cliffs that create a diffuse perimeter. Cliff heights of 30–70 m are common, containing over 30 sub-horizontal cliff and bench layers in some locations.

3.1.3. Thermal inertia

The thermal inertia values were obtained from processed and calibrated (Fergason et al., 2006) band 9 THEMIS images (Christensen et al., 2004). We examined THEMIS images acquired between years 2003–2004 (~ orbits 5000–12000, Mars years 26–27). Since surface temperatures vary seasonally, even images acquired at the same local time (pre-dawn) could differ by up to ~ 200 $Jm^{-2}K^{-1}s^{-1/2}$ (this study, and Baldridge et al., 2013). This uncertainty is expected, and the absolute difference in thermal inertias of various units was consistent across the images. Thus, we stretched the images in Fig. 20 to match the values in THEMIS I05975009 ($Ls = 171$, $Lt = 5$), and reported values in Table 5 based on this image. This scaling decision was not entirely arbitrary; we examined contemporary Mars Orbiter Camera (MOC) wide-angle (WAC) and narrow-angle (NAC) images to guide us to use THEMIS thermal inertia measurements from relatively quiet atmospheric periods with no indications of dust-storms or a lighter dustier surface.

The light-toned fan units had the lowest thermal inertia averages (150–240 $Jm^{-2}K^{-1}s^{-1/2}$). The neighboring highland units surrounding Hypanis to the south had slightly higher values (190–270 $Jm^{-2}K^{-1}s^{-1/2}$), and the dark-toned smooth ponded material in Lederberg crater had the highest values (270–390 $Jm^{-2}K^{-1}s^{-1/2}$).

3.1.4. Albedo

We found for both CTX images analyzed (F02_036517 and P17_007534) that histograms of albedos formed a normal bell-shaped curve centered at 0.18 and 0.20 respectively, and that the values ranged up to 0.02 from the mean. Estimated Lambertian albedos were ultimately recorded from CTX P17_007534 in Table 5.

3.1.5. Spectra

CRISM data in our study region were limited in coverage at higher resolution, and a map of CRISM footprints is shown in Fig. 21. If we assume that Hypanis is a deltaic deposit, then we might expect to find the best Fe/Mg clay signatures in the lowest strata along the distal front

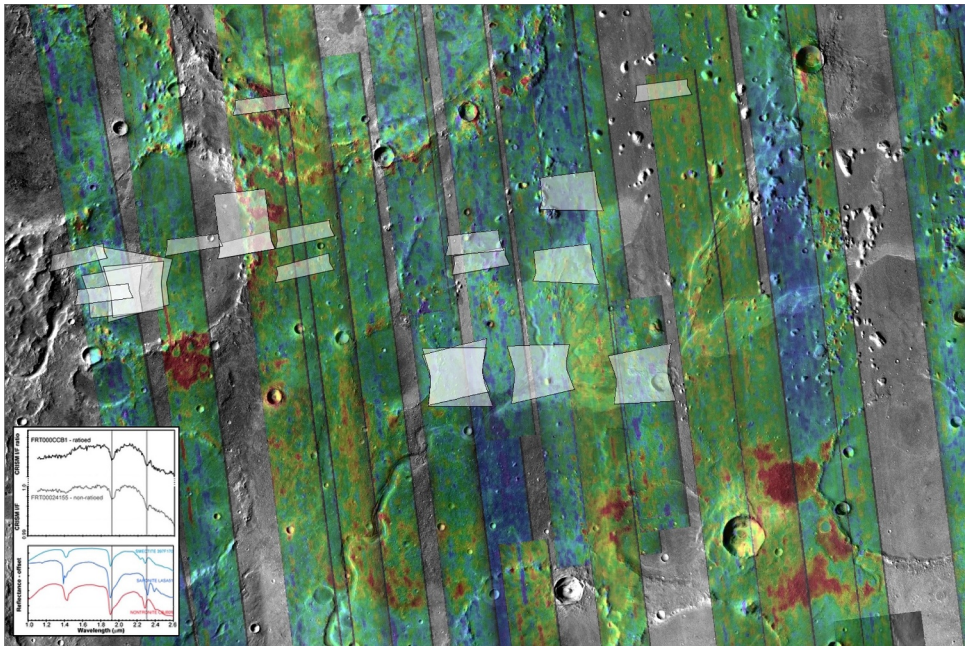

Fig. 21. Background: This qualitative D2300 (absorption strength at 2.3 microns) parameter map shows the distribution of potentially phyllosilicate (clay) bearing material in our study region. Individual image strips are low-resolution CRISM Multispectral Survey (MSP) products that have been atmospherically and photometrically corrected. Images are each 10 km wide and 200 m/pix. The numerical values have been stretched for each image individually from high absorption (red) to low (blue) and values are not necessarily consistent across different images. Foreground: The distribution of Full Resolution Targeted (FRT) and Full Resolution Short (FRS) CRISM spectral images are shown in white. Inset: For a quantitative approach, we examined spectra from these full-resolution images and compared to lab samples in the CRISM database. In general, we see very weak hydration signatures from the Hypanis deposit, which could be due to dust cover. We also found that the red regions in the low-resolution products, which likely have the highest hydration absorptions, have not been specifically targeted with CRISM/HiRISE yet. (For interpretation of the references to color in this figure, the reader is referred to the web version of this article.)

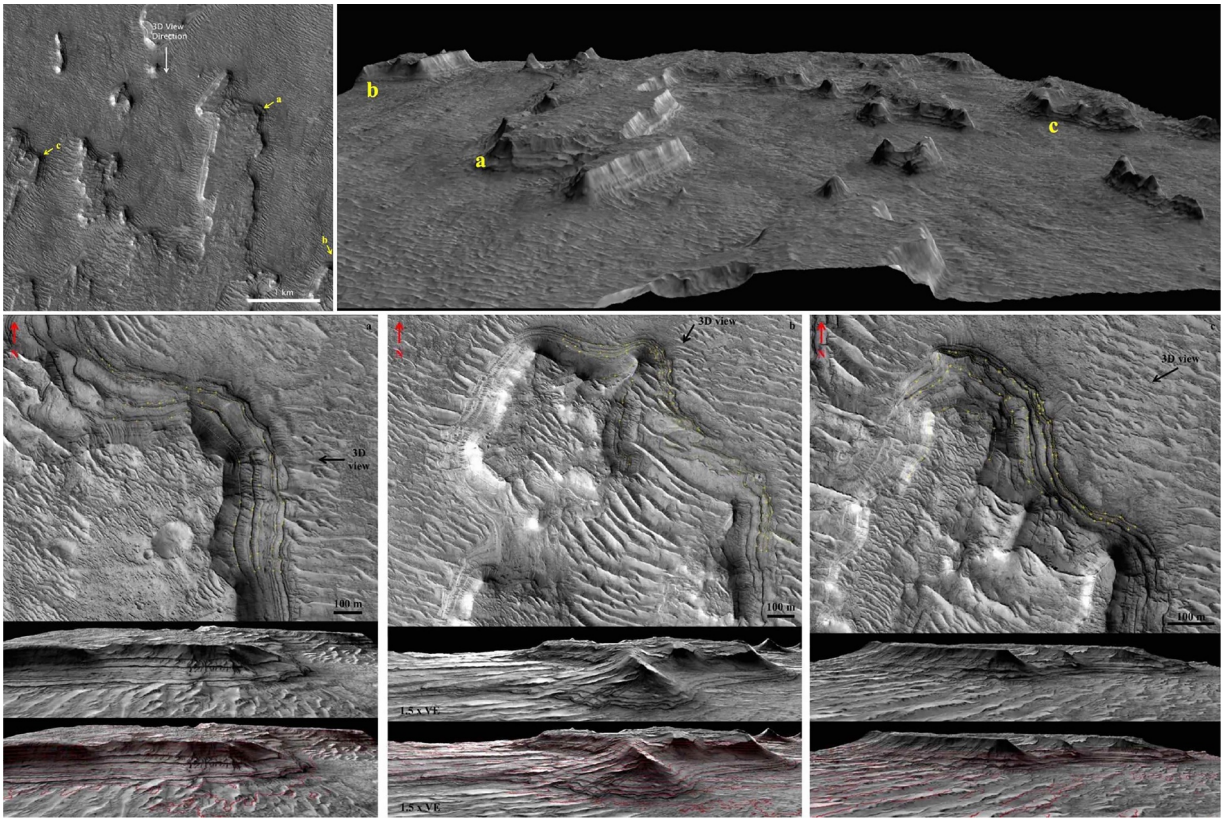

Fig. 22. The northern edge of main lobe (A) ends with cliffs roughly 70 m in height. Sun angle shadowing of the cliff and bench structure highlights the sedimentary layers in Hypanis. View (top right) is looking south at layering in the main lobe cliffs. In these images HiRISE image ESP_021577_1920 is overlaid on a HiRISE stereo DTM. Sample strike and dip measurement data points (yellow dots) trace around curved edges in the cliffs to better fit bed planes, and the resulting calculated dips are reported in Table 6. Red elevation contour lines also show that beds are nearly flat. (For interpretation of the references to color in this figure, the reader is referred to the web version of this article.)

exposures of the main lobe or channels. These areas were not covered by any higher resolution targeted CRISM sequences. We examined spectra from all CRISM cubes in Fig. 21, and found no strong signatures that would indicate igneous rocks, but some absorption features near 1.4, 1.9, and 2.3 microns implying hydration and the presence of Fe/Mg smectite clays. We identified several spatially coherent regions in the Hypanis vicinity (red regions, Fig. 21) with strong absorptions at 2.3 microns (D2300 parameter) from lower resolution CRISM MSP products. Where data are present, the bulk of hydration and clay signatures in the mapped region geographically correspond to crater rims and polygonally fractured terrain as seen in HiRISE images.

3.2. Formation processes tests

3.2.1. Main lobe

We evaluated formation hypotheses and list results in Tables 1 and 2. The main lobe of the Hypanis deposit consists of layered beds with gradients between 0–2° (Table 6 and Fig. 22). From our preliminary analysis, the northern front of the main lobe was most likely to contain cliffs with a stratigraphic record of depositional change. From our measurements in this region, we did not identify a change in slope that could indicate the interface of topset and foreset beds. However, we later discuss that this property might be unlikely to be testable after all due to the size of the potential deltaic deposit and the amount of erosion suggested by its present surface.

From visual examination of CTX images, we identified avulsion nodes at three different locations (Fig. 5). From our regional elevation mosaic we found that Hypanis is nestled in a topographic bay (Fig. 23) along the

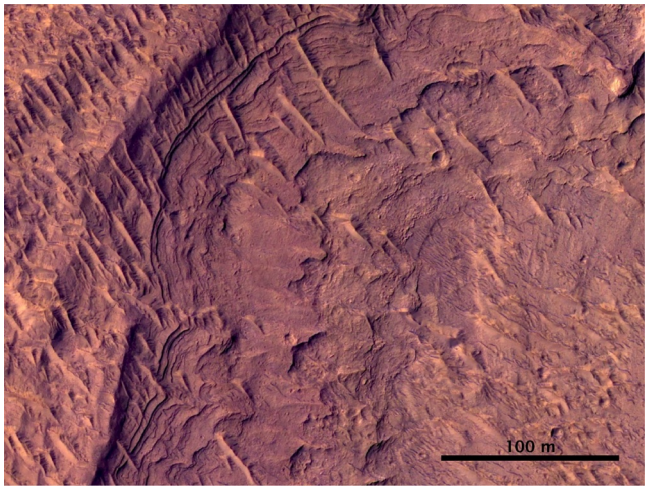

Fig. 23. Layers in Hypanis fan form small cliffs and terraces. HiRISE ESP_021577_1920, NASA/JPL/UA.

Table 6
Dip angles of layered beds along Hypanis front.

Cliff	Layer	Dip° ± Error	Dip Direction ± Error	Number of points	RMS error	R^2
A	1	0.34 ± 0.24	31.45 ± 45.73	9	0.24	66.21
	2	0.15 ± 0.27	59.32 ± 88.16	10	0.31	14.41
	3	0.56 ± 0.34	56.32 ± 30.41	8	0.22	67.91
	4	0.32 ± 0.11	85.34 ± 16.04	13	0.18	92.56
	5	0.32 ± 0.12	73.51 ± 20.00	8	0.13	95.33
B	1	1.06 ± 0.63	187.24 ± 105.90	7	0.76	86.54
	2	1.32 ± 0.39	97.03 ± 15.29	13	0.81	97.89
	3	1.30 ± 0.17	92.67 ± 6.64	16	0.35	99.46
	4	1.38 ± 0.53	93.69 ± 20.25	15	1.17	95.75
C	1	1.83 ± 1.05	65.24 ± 37.69	6	0.45	94.27
	2	1.03 ± 0.41	71.79 ± 23.69	16	0.55	74.21
	3	1.00 ± 0.43	39.55 ± 23.85	10	0.42	71.49
	4	1.61 ± 0.38	56.56 ± 12.25	14	0.24	82.89
	5	0.65 ± 0.56	35.47 ± 57.40	15	0.35	69.66
	6	1.23 ± 0.45	53.54 ± 19.10	8	0.10	85.14

Chryse escarpment, with lower elevations to the northeast. We searched the immediate surroundings of the Hypanis deposit for water strandlines, spectral signatures of byproducts of standing water, and other deltaic or lacustrine landforms which could provide cotemporaneous support for a standing body of water in this open basin. We found no additional support fromwithin the immediately surrounding basin, but several strong cases could be made for the greater region. These phenomena include the potential Sabrina delta (60 km to the west in Magong crater, with similar albedo, thermal inertia, apex elevation, and morphology to the Hypanis deposit, Hauber et al. (2009) and hydro-volcanic features in Lederberg crater (30 km north of the main lobe, Brož and Hauber (2013). Polygonal fractures in the darker units which make up the floor and cap units at Hypanis could also be indicative of past standing water over the entire region, as the associated clay signatures lead us to favor ice-wedging or desiccation/mud-cracking as the leading formation hypotheses for fractures in the darker unit (discussed later in Figs. 29 and 30).

Larger clasts were identified in the lowest exposed strata of the fan deposit in HiRISE images and anaglyphs (Figs. 18, 19, and 23). The majority of the remnant Hypanis deposit lies above these blockier beds and has no visible clasts at HiRISE resolution. These blockier layers are not associated with a higher THEMIS-derived thermal inertia as expected for boulders entrained in a conglomerate. In fact, no difference was detected between the thermal inertia of beds containing these blocks and beds without visible clasts, and the entire fan deposit exhibits a very low thermal inertia (150–240 $Jm^{-2}K^{-1}s^{-1/2}$) (Figs. 4f, 20, and Table 5). We searched all HiRISE digital elevation models and images for ridges bounding any light-toned layered sequence. We found no levees in the region, which often form during mudflows and can support channelized travel of high sediment loads to distant parts of the fan-deposit. We searched the MOLA global digital elevation model for a likely source for a mudflow and found none nearby. We show in Fig. 24 that the nearest potential sediment source in such a case is too distant to support the mudflow hypothesis.

We measured the along-flow and across-fan profiles of the main fan (Figs. 25 and 26) for overall slope and shape. The slope profile had

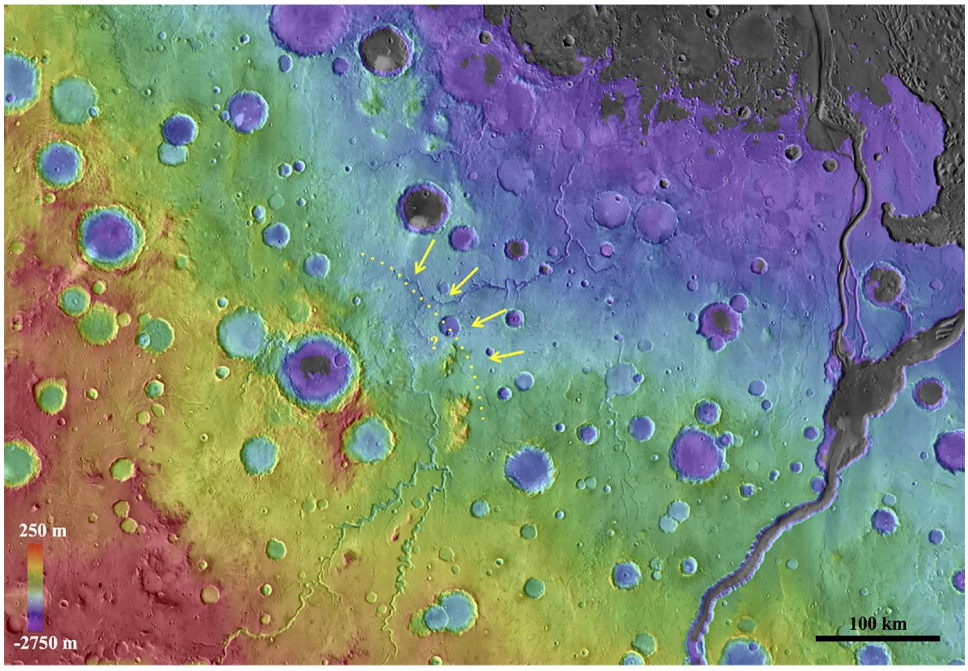

Fig. 24. If short-timescale repeated overland flow of mud was responsible for producing the layered Hypanis deposit, what would a likely source region be? We show a region bounded by a yellow curved line which is the nearest source of large relief and missing material, but travel of a mudflow over such a great distance is very unlikely. (For interpretation of the references to color in this figure, the reader is referred to the web version of this article.)

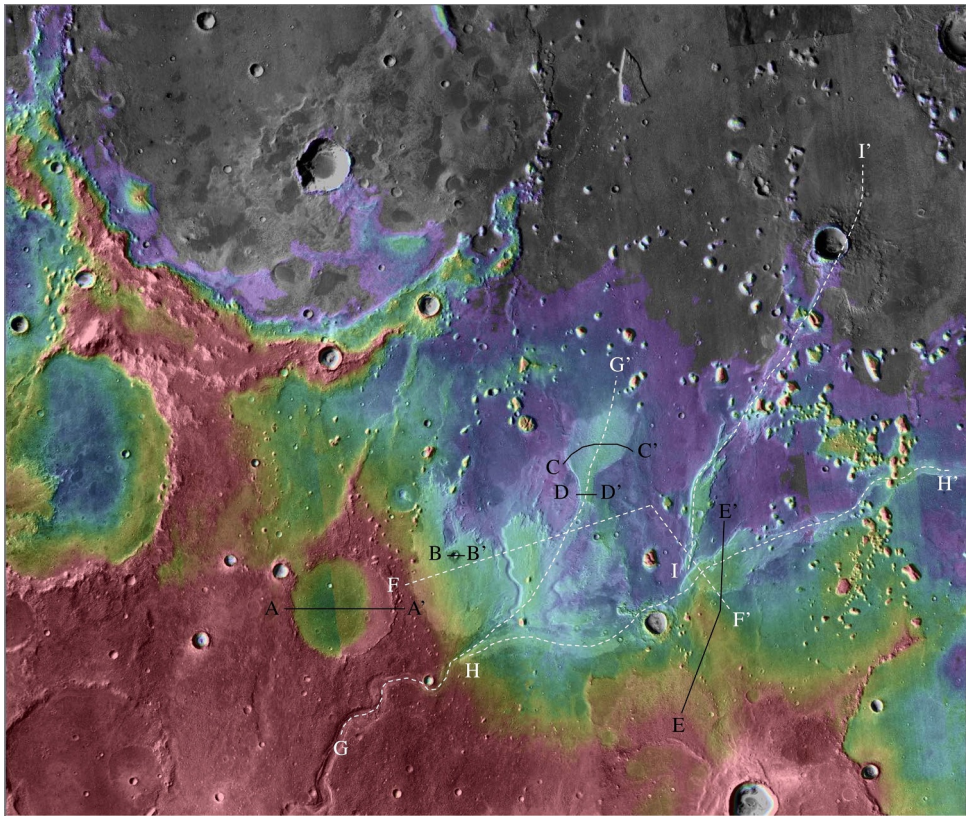

Fig. 25. Context map for elevation profiles. Profiles a-e marked in black are found in supplemental Fig. S3.

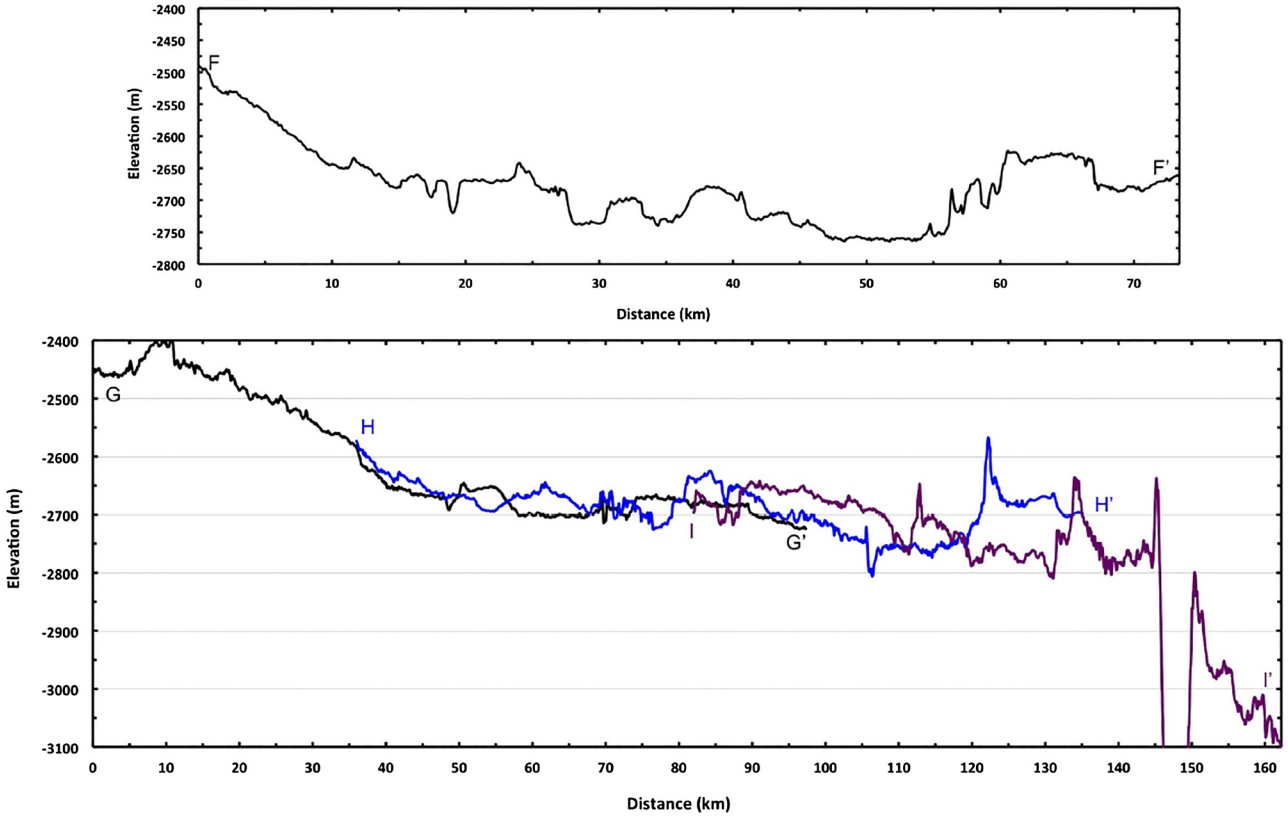

Fig. 26. Long elevation profiles show the topographic relationships between the lobes and inverted channels. The apex of the deposit begins around elevation -2550 m.

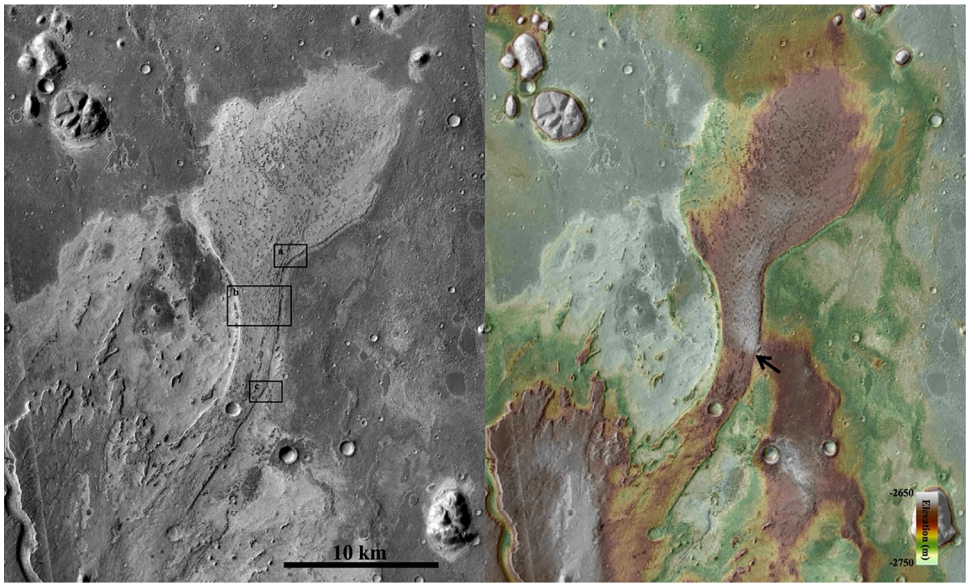

Fig. 27. The northern lobe of Hypanis displayed in a CTX image (left) and with our DEM mosaic overlay (right). Locations of Fig. 28 shown, and location of a 70 m bump in channel topography marked with black arrow.

a much lower gradient than expected for a classical alluvial fan (see slope distinction from Section 5 of Schon et al. (2012) and discussion in Wood (2006), but low gradients are not inconsistent with potentially analogous megafans on Earth, such as the Kosi or Okavango for instance (Stanistreet and McCarthy, 1993). As previously reported, the main lobe did not display a fixed avulsion node (Fig. 5), but a more complex alluvial/fluvial system could avulse for a number of reasons. We examined all HiRISE images of the layered deposit to assess the clast size distribution within the main lobe. One might expect in the classical alluvial fan case to find larger grains, cobbles, or boulders within recent channels. We found no evidence of boulders, but note that the 0.25 m/pixel resolution of HiRISE images means that we would not see boulders smaller than about 75 cm without favorable lighting conditions to cast a large shadow. Furthermore, we see no visible evidence of clasts of any size within the deposit.

3.2.2. Northern lobe

We observed that the northern lobe of the Hypanis deposit (Fig. 4c labeled B) does not consist of rocky units visible in HiRISE images, or a thermal inertia consistent with a rocky composition (thermal inertia calculated from THEMIS images I05975009 (Fig. 20) and (THEMIS image I16883014). We examined a HiRISE anaglyph and DEM (Fig. 27) of the northern lobe and did not find topographic signatures of a moraine at the foot of the lobe. The layers presumed to be within the northern lobe are indeed visible in the walls of the channel or neck, but are covered in many places by bedforms or talus from the ledges above (Fig. 28). We measured these beds with LayerTools and again found very low dip angles (less than 2°). These layers do not seem to conform with underlying topography. We determined from HiRISE images and our DEM that the shape was not consistent with either a rock glacier or dust-covered dirty glacier. Profiles plotted across the northern lobe showed that a rounded top (perhaps indicative of an esker) is not present (see supplemental Fig. S3). We examined our regional datasets and found no clear signs of contemporaneous glaciation.

We did not see any clasts or boulders in the HiRISE image of the northern lobe, and the low THEMIS thermal inertia possibly supports that there was not a large fresh rocky unit exposed at the surface. We noted that the source of a potential mudflow would be the same as for the main lobe (Fig. 24) which is too distant to be a likely mechanism. No levees were seen, which could have strongly supported a debris flow hypothesis.

The highest point of the northern lobe (-1650 m) occurs at its neck and is shaded white near the arrow in Fig. 27. We identified locations outside of the northern lobe and channel on the main deposit with elevations higher than −1650 m.

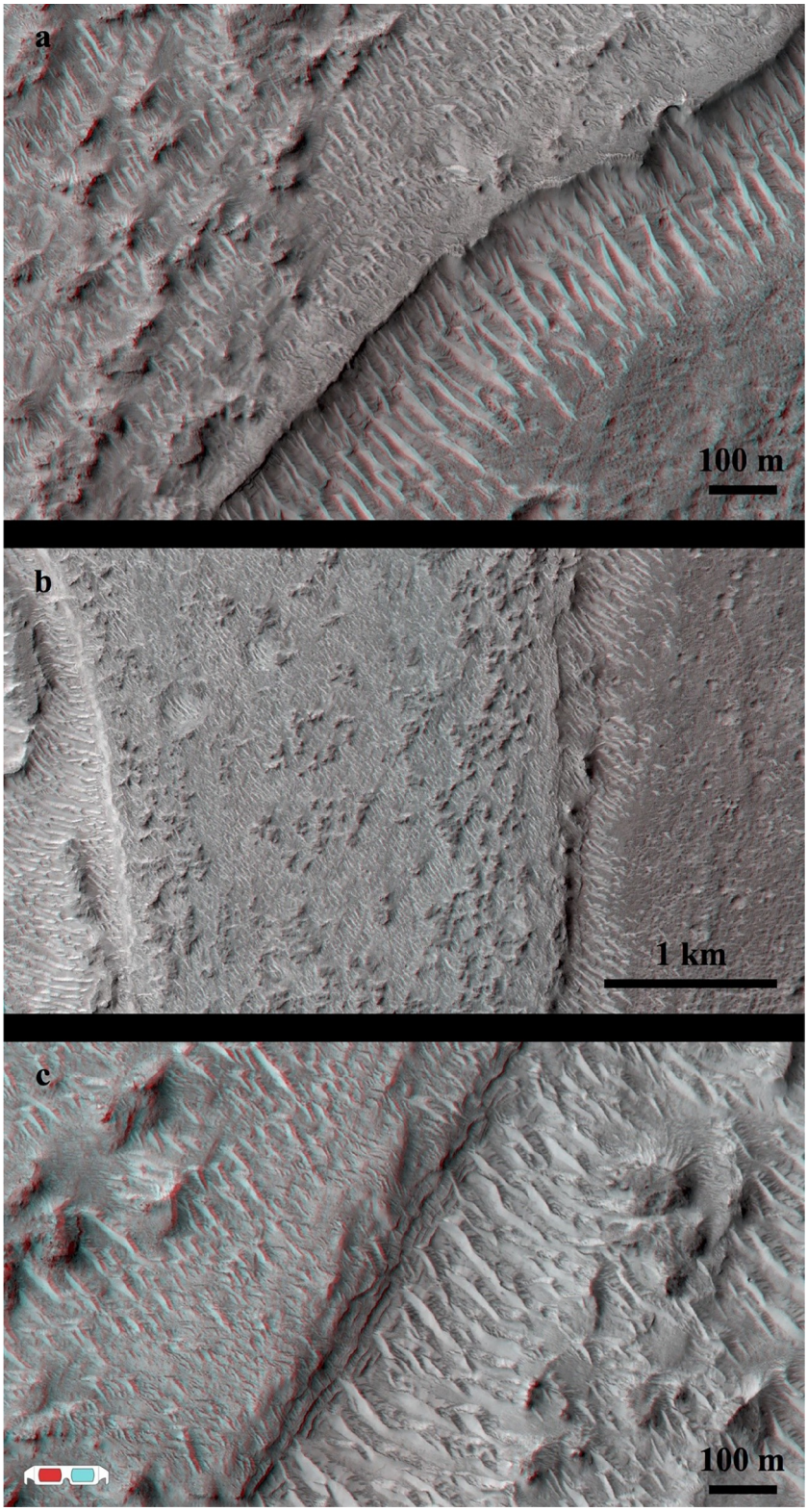

Fig. 28. HiRISE anaglyphs of the northern lobe: (a) fragments of a darker cap unit overlie the layered deposit. (b) darker material to the east, on top, and to the west of the neck of the northern lobe suggests a draping relationship postdating the lighter channel deposit. (c) sub-horizontal layers in the neck of the northern lobe are best exposed here, as farther north bedforms cover the lobe and create a blurred border.

4. Interpretations

Our results partially support a deltaic origin for the Hypanis deposit, and we favor this interpretation over the alluvial fan hypotheses. Our results do not support a mudflow origin. Low thermal inertia, thin sub-horizontal beds, and avulsion node migration are all consistent with an ancient deltaic environment along the Chryse escarpment. The lateral extent of these nearly flat beds over distances upwards of 10 km and their erosional morphology are indicative of a sedimentary lacustrine or marine process where finer clasts settle. The brighter albedo component

Table 7
Relative sizes of several commonly referenced deltas on Mars and Earth compared to the main lobe of Hypanis.

Delta Name	Approximate Area (km^2)
Jezero	60
Eberswalde	130
Sabrina	250
Hypanis	1,100
Colorado	1,600
Yellow	3,300
Kosi Megafan	9,900
Nile	32,000
Mekong	55,000
Mississippi	70,000

Approximate areas were measured in JMARS according to geologic maps and literature review. The main lobe of Hypanis is roughly comparable in size to the delta of the Colorado River at the Gulf of California, as well as other smaller river deltas on Earth (not listed). Hypanis is much larger than Jezero and Eberswalde, which both are believed to have formed in ponded craters or closed basins. Sabrina, in Magong crater, was included for reference as it likely formed by a similar process as Hypanis as noted in this work and in Hauber et al. (2009).

in the bedforms atop and at the base of the layered deposit is likely sourced from aeolian erosion of the light-toned beds and indicates that the fluvial units erode into sand- or silt-sized clasts. The variations in thermal inertia across the deposit surface likely represent the amount of aeolian bedforms present, and could be a sign of active erosion. The lowest thermal inertia values seem confined to the flanks of the light-toned deposit and to the flats beyond the main lobe front cliffs where locally sourced fine grain bedforms cover the deposit.

Our results from the distal northern lobe tests strongly support a fluvial origin; the northern lobe could have been formed in a typical fashion of fans and deltas, with new channels incising into a higher standing main lobe, and sediment being carried farther down-gradient until deposition on top of older deposits. We believe the northern lobe is part of the delta structure, and not formed by a different process.

We believe the distal island deposits (E in Fig. 4c) were once part of either the main lobe (A) or the inverted braided channel (C). The matching thermal inertia, morphology, and albedo indicate that these remnant islands were once connected to the Hypanis fluvial system. The position of these distal deposits could have been linked to channel C if flow had meandered north of its current path, or been related to main lobe A. The diffuse northern border of the main lobe (with abrupt cliff faces and visual signs of high levels of erosion) indicates that the deposit was once larger. The basin floor topography from the main deposit northward is not currently blocked, and the distal islands stand 10–15 m higher than their surroundings. If these distal deposits were part of the main lobe, a delta at Hypanis would have been over 130 km in length. Even if these deposits were not part of the main lobe, the Hypanis delta main lobe (A as mapped in Fig. 4c) is still the largest potential delta identified to date on Mars. The main lobe alone is ~ 40 km in length, spans an area just over 1,000 km^2, and has a sediment volume of ~ 80 km^3. The main lobe area alone (excluding the distal northern lobe, inverted channels, and distal island deposits) is comparable to small river deltas on Earth, such as the Colorado River Delta at the Gulf of California, but is dwarfed by the aerial extent of deltas like The Nile, about 30 times its size (Table 7).

Based on our topographic analysis and cross-cutting relationships, we interpret that the main lobe (A) formed subaqueously first and was much larger than its current area. Then the northern lobe (B) formed as the shore receded to the north. The water level retreated further and braided inverted channels C then D formed subaerially, leading downslope toward a lower shoreline.

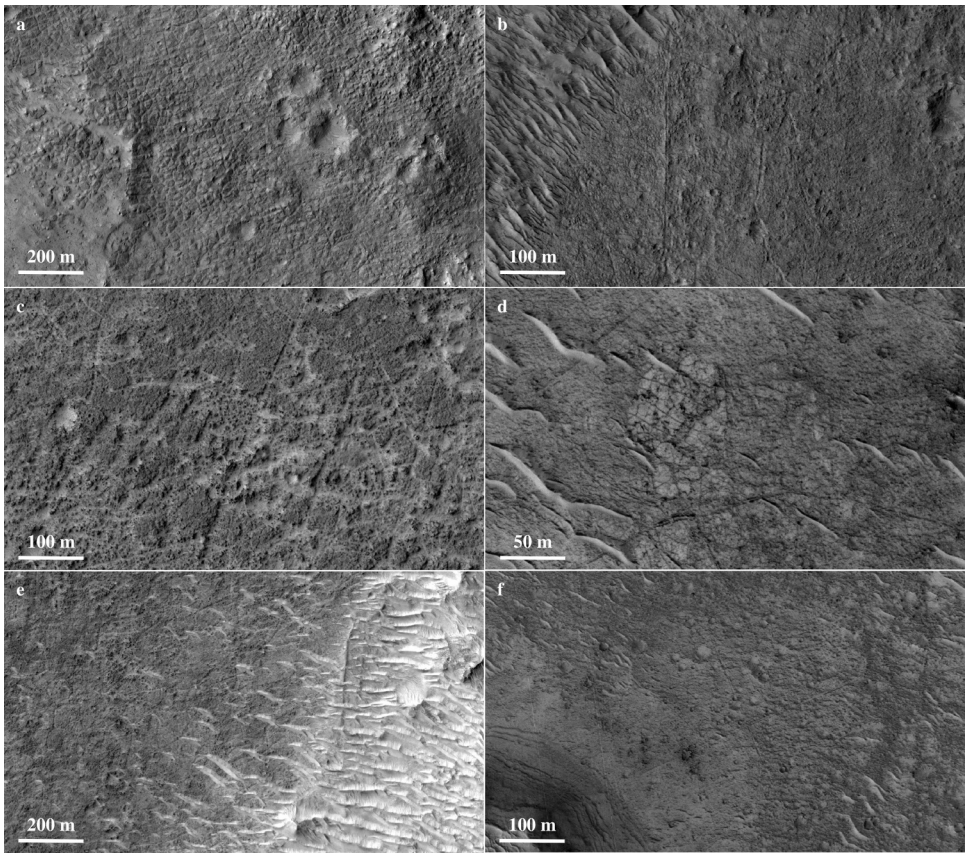

Fig. 29. The darker floor units surrounding Hypanis are, in some places, fractured polygonally or orthogonally. Linear to curvilinear floor fractures extend several kilometers in some cases, and appear at various stages of either formation or exhumation/degradation. Our leading hypotheses for formation of these features is ice-wedging/periglacial processes, or desiccation. The locations of these example polygons and fractures are shown in Fig. 4a. (a) A large field of similarly sized polygons near an impact crater ejecta blanket (see Fig. 4a) fades into a more linear fracture pattern towards the north edge of the image. (b) Orthogonal or zipper-like fractured terrain at the base of the channel C deposit. The large N-S trending fracture consists of two raised ridges and a central trough. (c) A fractured floor region appears to be in an eroded state. (d) A localized lighter unit exhibits a different fracture pattern than its surroundings. (e) Fractures in the darker floor unit at the base of the northern lobe. (f) A large orthogonal cross pattern at the base of the Hypanis layered deposit is perhaps representative of a different process than that which created polygonal terrain.

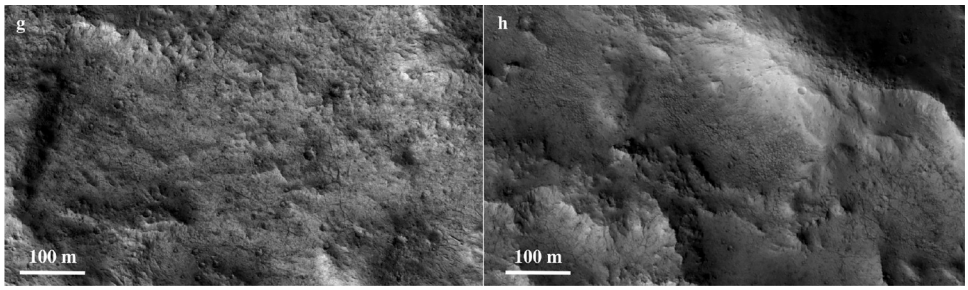

Fig. 30. Polygonally fractured units are found as far as the Lederberg crater rim. HiRISE ESP_047805_1925. (g) Depicted is the region from Fig. 31 (yellow box) with a strong signature of Fe/Mg phyllosilicate-bearing material, identified in a CRISM full resolution image. This terrain corresponds clearly with polygonal fractures. We extrapolate that other example locations with similar fractures, but lacking CRISM coverage, might also be phyllosilicate-bearing. (h) small-scale polygons within the Lederberg crater rim.

We interpret the darker surrounding floor units and dark patchy cap unit to be younger Hesperian volcanic or volcani-sedimentary deposits. Although the lower resolution global geologic map of Mars (Tanaka et al., 2014) marks this region as late Noachian highlands, this unit more closely resembles the neighboring unit to the north (early Hesperian transition unit) with its N-S trending wrinkle ridges. Although only marginally darker in measured albedo, these units are morphologically quite different. They retain small craters (see Edgett, 2009 and lie topographically above the flat deltaic beds. They appear to embay the light-toned deposits and in some areas show signs of deflation. The darker units also are found in some places to slope up onto (onlap) the deltaic deposit and cover its top surface. The presence of volcanic or volcaniclastic deposits in this broader region to the north of Hypanis is well documented by both the Viking 1 and Pathfinder data, and this darker younger unit is perhaps characteristic of the local eHt (early Hesperian transition) unit mapped by Tanaka et al. (2014), which appropriately contains a moderate amount of wrinkle ridges and some volcanic deposits in places.

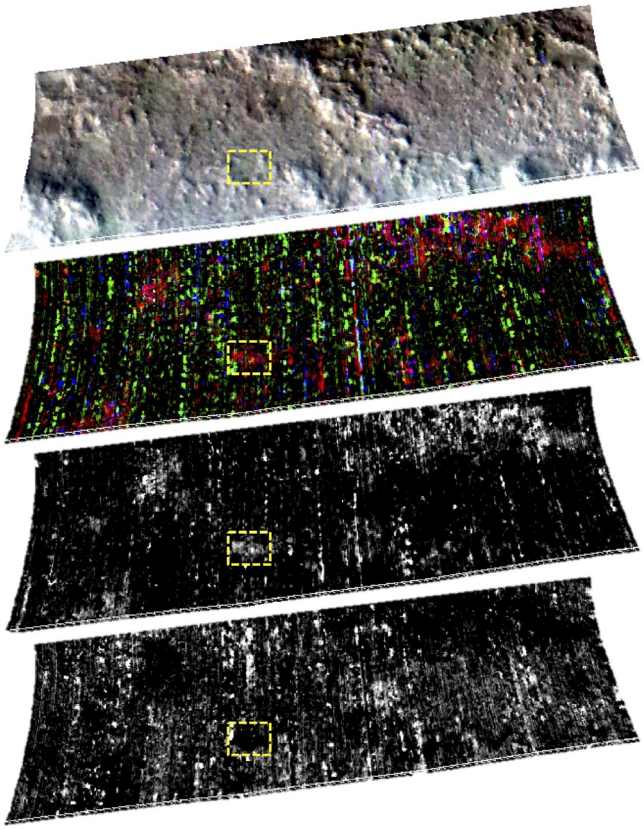

Fig. 31. CRISM observation FRS0003F079 parameter images (described in Viviano-Beck et al., 2014) within Lederberg crater rim. From top to bottom: a) False color browse product image R:2529, G:1506, B:1080 b) Phyllosilicate browse product (PHY) R:D2300 [0.00-0.01], G:D2200 [0.00-0.01], B:BD1900r2 [0.00-0.01] c) 2.3 micron band depth parameter (D2300) [0.00-0.01] d) Low-calcium pyroxene parameter (LCP Index) [0.00-0.01]. The bright regions in (c) have a 1% dip in the reflected spectrum at 2.3 microns. This absorption is typical of several Fe/Mg-bearing phyllosilicate clays, which are the most common hydrous mineral on Mars [Carter et al. (2013b)]. The browse product recreated in image (b) confirms the presence of Fe/Mg-OH bearing minerals in red or magenta when hydrated. The greenish hues in (a) approximately match the detections in (b) and (c). The yellow dashed box shows the location of Fig. 31g. (For interpretation of the references to color in this figure legend, the reader is referred to the web version of this article.)

These darker units also display polygonal, orthogonal, and zipper-like fracturing (Fig. 29). We found patches of this polygonally fractured terrain as far as the Lederberg crater rim (Fig. 30). We posit that these fractures (and polygons above ~ 2 m in size) are likely a result of freeze-thaw action or ice wedging. Smaller polygons in the region are often associated with CRISM smectite clay signatures (Fig. 31). We posit that these fractures were created by desiccation. As it appears that there were several flows emplacing these darker surrounding units, and since the albedo of these units are very similar, we have not yet tried to separately describe flow events, compositional differences, or fracture processes within this broader dark wrinkle ridge containing unit. Since this unit appears to be an eroding cap on top of the northern lobe deposit, we believe the darker unit likely covered all of the Hypanis deposit, and perhaps helped shelter and preserve the sedimentary units from the regional catastrophic erosion of ~ 3.2 Ga.

5. Discussion

Despite the lack of clear evidence of an angular unconformity (with topset beds above foresets at a higher slope) we believe it would be unlikely to affirm this test given the large size and severe state of erosion of the ancient Hypanis deposit. Smaller and/or steeper deltaic deposits may benefit from subjection to this test. Also, not all types of deltas would have superposing beds with contrasting dipping angles like this (Coe, 2003). It could also be possible that the majority of the beds measured were bottomset or topset beds, but without a higher resolution oblique view of the deposit cliffs, the clast size distribution within a layer is hard to discern. (Similarly, if a large active terrestrial delta dried and lithified, it is unclear whether we would be able to identify topset and foreset beds from the same orbital assets we currently have at Mars.)

We marked the test of additional support of a standing body of water as Maybe (Table 1) due to the strong similarity of Hypanis to the potential delta in Magong crater (Hauber et al., 2009), the similarity in elevation of other potential deltas (Di Achille and Hynek, 2010a), and the proximity of hydro-volcanic features (Brož and Hauber, 2013). Our spectral analysis also supports a Chryse ring of hydrated minerals presented by Carter et al., (2015a) near these elevations. The polygonal fractures in the floor unit at the base of Hypanis are strikingly similar to those at the base of the potential Martian delta in Jezero crater (W. Abbey, pers. comm.). Perhaps this indicates a similar depositional environment.

A theoretical argument could still be made for Hypanis being a low gradient alluvial fan composed of mudflows. We assigned the result of

Maybe for the test of the characteristic shape and morphology of an alluvial fan (Table 1), since alluvial fans could consist of sand and mud. While terrestrial examples of low gradient fine grain mudfans do exist, none to our knowledge resemble suitable analogs of the complex morphology of the Hypanis deposit.

If our favored hypothesis of a deltaic environment is correct, the amount of water required to fill the portion of Chryse spanned by Hypanis is not trivial. A lake of 100 km in length is perhaps the minimum size of a body of water that could have housed the large delta. Our analysis supports the idea of an even larger body of water in Chryse planitia, and potentially a northern ocean on Mars, and would be consistent with proposed shorelines by Clifford and Parker (2001), Di Achille and Hynek (2010a), and Rodriguez et al. (2015).

A potential ocean is supported by other bodies of work as well. Baker et al. (1991) argued that many geomorphological features could be explained by an episodic northern ocean (Oceanus Borealis) and ice-sheet formation. Lucchitta (1993) added that geomorphic features in the northern hemisphere would also be consistent with an ice covered polar lake or ocean, which could even be completely frozen. Parker (1994) proposed two traceable paleoshorelines, which were again tested with MOLA data by Head et al. (1998). The later results were consistent with the hypothesis of a large standing body of water in the northern lowlands of Mars since Head et al. (1998) found smoothing at all length scales below Parkers younger Contact 2, that the contact was a close approximation to an equipotential surface, and the enclosed volume was consistent with total outflow channel discharge and maximum estimated megaregolith pore space. Malin and Edgett (1999) analyzed MOC images specifically targeted to re-examine terrain previously argued to support an ocean coastline, but found no evidence to support the shorelines previously proposed. Clifford and Parker (1999) posited that the existence of a primordial ocean on Mars was an inevitable consequence of the hydraulic and thermal conditions that existed during the Early Noachian. Carr (2000) suggested that while 1.5 m/pix MOC images did not support identification of shoreline features, other new images of valleys strongly support sustained or episodic flow of water over the surface, and high erosion rates could support a warm climate and presence of large bodies of water during heavy bombardment. Clifford and Parker (2001) further summarized hydraulic and thermal conditions could imply the northern surface was covered with standing bodies of water and ice. Fig. 6 in Clifford and Parker (2001) marks the Arabian Shoreline globally, which matches the locations of Hypanis and Sabrina along the Chryse escarpment. Di Achille and Hynek (2010a), as previously discussed, mapped an equipotential surface based on the elevations of valleys and a list of potential deltaic deposits, which is consistent with our analysis at Hypanis. Fig. 3 in Rodriguez et al. (2015) also draws a shoreline during the Late Noachian based on the geomorphology of valleys and craters that is again consistent with the location of Hypanis. Recent work by Citron et al. (2018) is also relevant to northern plains water bodies. If Hypanis is much older than the reported 3.6 Ga, then it could fit their proposed model of an earlier Arabia shoreline. If 3.6 Ga is an accurate age for Hypanis, then perhaps Hypanis would instead fit into a model of the Deuteronilus paleoshoreline, belonging to a body of water after Tharsis and true polar wander could have warped Martian topography. Recent work by Rodriguez et al. (2016) shows that bolides hitting a northern body of water can create tsunami deposits. While we might expect to see the same effects, we have not yet found evidence of these types of deposits in our study region, which is farther south and at a higher elevation than the units found in Rodriguez et al. (2016).

Although not as strongly supported by current topography, it is also possible that Hypanis was deposited into a more confined closed basin, with a northern border which has since disappeared. Either a glacial dam or a land dam could have ponded the water into which Hypanis formed. During periods of high obliquity, glacial ice migrated to the mid latitudes of Mars, and possibly as far as the equator. According to the Late Noachian Icy Highlands (LNIH) model (Fastook and Head, 2015), it is possible that early Mars was cold and icy rather than warm and wet, and top down melting of ice sheets can account for widespread valley network formation. Even without invoking this climate model, large obliquity shifts alone could create ice deposits at 14° N over 3.6 billion years ago (Mellon and Jakosky, 1995; Laskar et al., 2004). Ice to the north could have created a closed basin topography, but the delta sediments were still sourced from the Noachian highlands to the south (by either groundwater, precipitation led surface runoff, or glacial melting). While our specific landform tests in Table 2 were negative for ice-related processes, we cannot rule out that ice was not present in the region at that time. It is also possible that our topographic test for eskers was inadequate, as 3 billions years of erosion, burial, and exhumation could reduce a rounded top to a flat top. Evidence of regional icy regolith in the form of impact craters with slurry rampart ejecta (black arrows Fig. 4f; Reiss et al., 2006 is common in the region, but appears to stratigraphically post-date Hypanis.

A land dam could also have existed north of Hypanis. A plethora of rounded buttes dot the northern portion of our study region and are frequently arranged in a circular pattern interpreted to be former large impact crater rims. It is not impossible that crater walls once formed a closed basin before failing due to river incision, catastrophic flooding, aeolian abrasion, or other gradational processes.

6. Conclusion

We used high-resolution orbital images, thermal IR images, and topographic data to assess the deposit at the terminus of Hypanis Valles along the edge of the Chryse basin. We favor a deltaic origin for the deposit over a mudflow or alluvial fan hypothesis. The implication of our proposed subaqueous formation is that a large body of water was present in the Chryse basin during the late Noachian. This deltaic deposit was then capped by a darker unit, which has subsequently been eroded. Hypanis is the largest potential delta on Mars to date, and its position along the edge of the northern lowlands is consistent with proposed paleo-shorelines of a northern ocean.

Acknowledgements

This work was supported by grants from the NASA Mars Odyssey Project under a subcontract to ASU administered by the Jet Propulsion Laboratory/California Institute of Technology. JD gratefully acknowledges NASA/ASU and UK Space Agency (UK SA) funding (ST/K502388/1, ST/R002355/1). ES-N and PF thank the UK SA and the STFC for supporting science relating to ExoMars Rover landing site selection activities through the following grants ST/L00643X/1 (PF, ES-N), ST/R001413/1 (PF). JA would like to thank Dr. Edwin Kite for providing feedback to improve this paper. We would also like to thank Lauren Edgar, Ryan Anderson, Phil Christensen, Kelin Whipple, Vic Baker, and an anonymous reviewer for helpful suggestions.

Supplementary material

Supplementary material associated with this article can be found, in the online version, at doi:10.1016/j.icarus.2018.05.021.

References

Adler, J.B., et al., 2016. Geologic stratigraphy, delta morphology, and regional history of hypanis delta. Mars. American Geophysical Union (Fall) Abstract # P11E-03.
Adler, J.B., et al., 2017. fluvial stratigraphy and regional volcanism at hypanis delta. Proceedings of the Lunar and Planetary Science Conference.
Anderson, J.A., et al., 2004. Modernization of the Integrated Software for Imagers and Spectrometers. Proceedings of the Lunar and Planetary Science Abstract #2039.
Anderson, R.B., Bell, J.F., 2010. Geologic mapping and characterization of gale crater and implications for its potential as a mars science laboratory landing site. Mars 5, 76–128.
Anderson, R.S., Anderson, S.P., 2010. Geomorphology: The Mechanics and Chemistry of Landscapes. Cambridge University Press, UK.

Baker, V.R., et al., 1991. Ancient oceans, ice sheets and the hydrological cycle on Mars. Nature 352, 589–594.
Baldridge, A.M., et al., 2013. Searching at the right time of day: evidence for aqueous minerals in columbus crater with TES and THEMIS data. J. Geophys. Res. Planets 118, 179–189.
Bell, J.F., 2008. The Martian Surface: Composition, Mineralogy, and Physical Properties. Cambridge University Press, New York.
Bell, J.F., et al., 2013. Calibration and performance of the mars reconnaissance orbiter context camera (CTX). Int. J. Mars Sci. Explor. 8, 1–14.
Beyer, R.A., 2015. An introduction to the data and tools of planetary geomorphology. Geomorphology 240, 137–145.
Bibring, J.P., et al., 2006. Global mineralogical and aqueous mars history derived from OMEGA/mars express data. Science 312 (5772), 400–404.
Blackwelder, E., 1928. Mudflow as a geologic agent in semi-arid mountains. Geol. Soc. Am. Bull. 39, 465–483.
Blissenbach, E., 1954. Geology of alluvial fans in semiarid regions. Geologic. Soc. Of America Bull. 65 (2), 175–190.
Broxton, M.J., Edwards, L.J., 2008. The ames stereo pipeline: automated 3d surface reconstruction from orbital imagery. Proceedings of the Lunar and Planetary Science Conference Abstract #2419.
Brož, P., Hauber, E., 2013. Hydrovolcanic tuff rings and cones as indicators for phreatomagmatic explosive eruptions on. Mars. J. Geophys. Res. 118 (8), 1656–1675.
Buffington, E.C., 1952. Submarine natural levees. J. Geology 60, 473–479.
Bull, W.B., 1964. Alluvial Fans and Near-Surface Subsidence in Western Fresno County. California. Studies of Land Subsidence, Geol. Surv. Proffesional Paper 437-A.
Bull, W.B., 1977. The alluvial-fan environment. Progr. Phys. Geogr. Earth Environ. 1 (2), 222–270.
Cabrol, N.A., Grin, E.A., 1999. Distribution, classification, and ages of martian impact crater lakes. Icarus 142, 160–172.
Cabrol, N.A., Grin, E.A., 2001. The evolution of lacustrine environments on mars: is mars only hydrologically dormant? Icarus 149, 291–328.
Carr, M.H., 1996. Water on Mars. Oxford University Press, University of Michigan.
Carr, M.H., 2000. Martian oceans, valleys and climate. Astron. Geophys. 41 (3), 3.20–3.26.
Carr, M.H., Head III, J.W., 2010. Geologic history of mars. earth and plan. Sci. Let. 294 (3–4), 185–203.
Carter, J., et al., 2015a. Mineralogic context of the final four, circum-chyrse candidate landing sites for the exomars rover. Proceedings of the European Planatry Science Congress.
Carter, J., et al., 2015b. Widespread surface weathering on early mars: a case for a warmer and wetter climate. Icarus 248, 373–382.
Catuneanu, O., 2006. Principles of Sequence Stratigraphy. Elsevier Science, Amsterdam.
Christensen, P.R., et al., 2004. The thermal emission imaging system (THEMIS) for the mars 2001 odyssey mission. Spa. Sci. Rev. 110 (1), 85–130.
Christensen, P.R., et al., 2009. JMARS a Planetary GIS. American Geophysical Union (Fall) Abstract #IN22A-06.
Citron, R.I., et al., 2018. Timing of oceans on mars from shoreline deformation. Nature 555, 643–646.
Clifford, S.M., Parker, T.J., 1999. Hydraulic and thermal arguments regarding the existence and fate of a primordial martian ocean. Proceedings of the Lunar and Planetary Science Conference Abstract #1619.
Clifford, S.M., Parker, T.J., 2001. The evolution of the martian hydrosphere: implications for the fate of a primordial ocean and the current state of the northern plains. Icarus 154, 40–79.
Coe, A.L., 2003. The Sedimentary Record of Sea-Level Change. Cambridge University Press, New York.
Craddock, R.A., et al., 1997. Geology of central chryse planitia and the viking 1 landing site: implications for the mars pathfinder mission. J. Geophys. Res.:Planets 102 (E2), 4161–4183.
Crumpler, L.S., 1997. Geotraverse from xanthe terra to chryse planitia: viking 1 lander region. Mars. J. Geophys. Res. 102 (E2), 4201–4218.
Di Achille, G., Hynek, B.M., 2010a. Ancient ocean on mars supported by global distribution of deltas and valleys. Nat Geosci 3, 459–463.
Di Achille, G., Hynek, B.M., 2010b. Deltas and valley networks on mars: implications for a global hydrosphere. In: Cabrol, N.A., Grin, E. (Eds.), Chapter 8 from Lakes on Mars. Elsevier Science.
Eckes, S.W., et al., 2016. Timing of fluvial activity in the xanthe terra region of mars: implications for hypanis delta, a potential landing site for mars2020. Proceedings of the Lunar and Planetary Science Conference Abstract #2196.
Edgett, K.S., 2009. MRO CTX and MGS MOC observations regarding small impact craters and substrate resistance to erosion on mars. AAS/Division for Planatry Science Meeting, Abstract #58.06.
Ehlmann, B.L., Edwards, C.S., 2014. Mineralogy of the martian surface. Ann. Rev. Earth Plan. Sci. 42, 291–315.
Fassett, C.I., Head III, J.W., 2008. The timing of martian valley network activity: constraints from buffered crater counting. Icarus 195, 61–89.
Fastook, J.L., Head, J.W., 2015. Glaciation in the late noachian icy highlands: ice accumulation, distribution, flow rates, basal melting, and top-down melting rates and patterns. Planet. pace Sci. 106, 82–98.
Fawdon, P., et al., 2018a. Hypanis valles delta: the last high-stand of a sea on early mars. Proceedings of the Lunar and Planetary Science Abstract #2839.
Fawdon, P., et al., 2018b. Hypanis valles delta: the last high stand of an ocean on early mars? [in press, Earth and Planetary Science Letters].
Fergason, R.L., et al., 2006. High-resolution thermal inertia derived from the thermal emission imaging system (THEMIS): thermal model and applications. J. Geophys. Res.:Planets 111 (E12), E12004.
Galloway, W.E., 1975. Process Framework for Describing the Morphologic and Stratigraphic Evolution of Deltaic Depositional Systems. Society of Economic Paleontologists and Mineralogist, Special Publication. pp. 127–156. No. 31
Ganti, V., et al., 2014. Testing morphodynamic controls on the location and frequency of river avulsions on fans versus deltas: huanghe (yellow river). China. Geophys. Res. Let. 41 (22), 7882–7890.
Goudge, T.A., et al., 2017. Sedimentological evidence for a deltaic origin of the western fan deposit in jezero crater, mars and implications for future exploration. Earth and Plan. Sci. Lett. 458, 357–365.
Goudge, T.A., et al., 2018. Stratigraphy and paleohydrology of delta channel deposits, jezero crater, mars. Icarus 301, 58–75.
Greeley, R., et al., 1977. Geology of chryse planitia. J. Geophys. Res. 82 (28), 4093–4109.
Grindrod, P.M., Warner, N.H., 2014. Erosion rate and previous extent of interior layered deposits on mars revealed by obstructed landslides. Geology 42 (9), 795–798.
Gupta, S., et al., 2015a. Hypanis: a deltaic-lacustrine system at the edge of a chryse sea? Proceedings of the 2nd Mars 2020 Landing Site Selection Workshop.
Gupta, S., et al., 2015b. The hypanis fluvial-deltaic-lacustrine system in xanthe terra. First Landing Site/Exploration Zone Workshop for Human Missions to the Surface of Mars Abstract #1051.
Hardgrove, C., Moersch, J., Whisner, S., 2009. Thermal imaging of alluvial fans: a new technique for remote classification of sedimentary features. Earth Plan. Sci. Lett. 285 (1–2), 124–130.
Hardgrove, C., Moersch, J., Whisner, S., 2010. Thermal imaging of sedimentary features on alluvial fans. Planet. Space Sci. 58 (4), 482–508.
Harrison, T.N., 2012. Evidence for volcanism in and near the chaotic terrains east of valles marineris. Proceedings of the Lunar and Planetary Science Conference Abstract #1057.
Harvey, A.M., Mather, A.E., Stokes, M., 2005. Alluvial fans: geomorphology, sedimentology. Dynamics Geological Society. Special Publications, London, pp. 1–7. 251
Hauber, E., et al., 2005. Delta-like deposits in Xanthe terra, mars, as seen with the high resolution stereo camera (HRSC). Proceedings of the Lunar and Planetary Science Conference Abstract #1661.
Hauber, E., et al., 2009. Sedimentary deposits in Xanthe terra: implications for the ancient climate on. Mars. Plan. Space Sci. 57 (8–9), 944–957.
Hauber, E., et al., 2013. Asynchronous formation of Hesperian and amazonian aged deltas on mars and implications for climate. J. Geophys. Res.:Planets 118 (7), 1529–1544.
Head, J.W., et al., 1998. Oceans in the past history of mars: tests for their presence using mars orbiter laser altimeter (MOLA) data. Geophys. Res. Let. 25 (24), 4401–4404.
Kite, E.S., Mayer, D.P., 2017. Mars sedimentary rock erosion rates constrained using crater counts, with applications to organic-matter preservation and to the global dust cycle. Icarus 286, 212–222.
Kleinhans, M.G., et al., 2010. Palaeoflow reconstruction from fan delta morphology on. Mars. Earth Planet. Sci. Let. 294 (3–4), 378–392.
Kneissl, T., et al., 2010. Measurement of strike and dip of geologic layers from remote sensing data—new software tool for arcGIS. Proceedings of the Lunar and Planetary Science Conference Abstract #1640.
Laskar, J., et al., 2004. Long term evolution and chaotic diffusion of the insolation quantities of mars. Icarus 170 (2), 343–364.
Lewis, K.W., Aharonson, O., 2006. Stratigraphic analysis of the distributary fan in eberswalde crater using stereo imagery. J. Geophys. Res.:Planets 111 (E6), E06001.
Loizeau, D., et al., 2007. Phyllosilicates in the mawrth vallis region of mars. J. Geophys. Res.:Planets 112 (E8), E08S08.
Lucchitta, B.K., 1993. Ice in the Northern Plains: Relic of a Frozen Ocean? LPI Technical Report 93-04, Part1, 9.
Malin, M.C., et al., 2007. Context camera investigation on board the mars reconnaissance orbiter. J. Geophys. Res. 112 (E5), E05S04.
Malin, M.C., Edgett, K.S., 1999. Oceans or seas in the martian northern lowlands: high resolution imaging tests of proposed coastlines. Geophys. Res. Let. 26 (19), 3049–3052.
Malin, M.C., Edgett, K.S., 2003. Evidence for persistent flow and aqueous sedimentation on early mars. Science 302 (5652), 1931–1934.
McEwen, A., et al., 2007. Mars reconnaissance orbiter's high resolution imaging science experiment (hiRISE). J. Geophys. Res.:Planets 112 (E5).
Mellon, M.T., Jakosky, B.M., 1995. The distribution and behavior of martian ground ice during past and present epochs. J. Geophys. Res.:Planets 100 (E6), 11781–11799.
Metz, J.M., 2009. Sublacustrine depositional fans in southwest melas chasma. J. Geophys. Res.:Planets 114 (E10), E10002.
Moore, J.M., Howard, A.D., 2005. Large alluvial fans on mars. J. Geophys. Res.:Planets 110 (E4), E04005.
Moratto, Z.M., et al., 2010. Ames stereo pipeline, NASA'S open source automated stereogrammetry software. Proceedings of the Lunar and Planetary Science Conference Abstract #2364.
Murchie, S., et al., 2007. Compact reconnaissance imaging spectrometer for mars (CRISM) on mars reconnaissance orbiter (MRO). J. Geophys. Res.:Planets 112 (E5), E05S03.
Nelson, D.M., Greeley, R., 1999. Geology of xanthe terra outflow channels and the mars pathfinder landing site. J. Geophys. Res.:Planets 104 (E4), 8653–8669.
Neukum, G., Jaumann, R., 2004. HRSC: the high resolution stereo camera of mars express. In: Wilson, A. (Ed.), Mars Express: The Scientific Payload. Noordwijk, Netherlands, pp. 17–35. ESA SP-1240
O'Shea, M.J., et al., 2016. Using the Morphology of Impact Craters as a Relative Age Indicator for Fluvial Activity at Xanthe Terra, Mars. Proceedings of the Lunar and Planetary Science Conference Abstract #1549.
Parker, T.J., 1994. Martian Paleolakes and Oceans. University of Southern California Phd thesis.
Piatek, J.L., Hardgrove, C., Moersch, J.E., 2007. Potential rock glaciers on mars:

comparison with terrestrial analogs. Proceedings of the Seventh International Conference on Mars Abstract #3353.
Platz, T., et al., 2014. Landing at the terminus of sabrina vallis: a potential 2020 mars rover landing site. EPSC Abstracts 9, 2014–2811. EPSC
Reiss, D., et al., 2006. Ages of rampart craters in equatorial regions on mars: implications for the past and present distribution of ground ice. Meteorit. Planet. Sci. 41 (10), 1437–1452.
Rice, M.S., et al., 2013. A detailed geologic characterization of eberswalde crater, Mars. Mars 8, 15–57.
Rodriguez, J.A.P., et al., 2007. Formation and disruption of aquifers in southwestern chryse planitia, mars. Icarus 191, 545–567.
Rodriguez, J.A.P., et al., 2015. Martian outflow channels: how did their source aquifers form, and why did they drain so rapidly? Nat. Sci. Rep. 5, 13404.
Rodriguez, J.A.P., et al., 2016. Tsunami waves extensively resurfaced the shorelines of a receding, early martian ocean. Sci. Rep. 6, 25106.
Rotto, S.L., Tanaka, K.L., 1989. Geologic Map of the Chryse Planitia Region. U.S. Geological Survey Map I-2441.
Salvatore, M.R., et al., 2010. Definitive evidence of hesperian basalt in acidalia and chryse planitiae. J. Geophys. Res.:Planets 115, E07005.
Salvatore, M.R., et al., 2016. The geologic history of margaritifer basin, mars. J. Geophys. Res.:Planets 121 (3), 273–295.
Schon, S.C., Head, J.W., Fassett, C.I., 2012. An overfilled lacustrine system and progradational delta in jezero crater. Mars: Implications for Noachian climate. PSS 67, 28–45.
Seelos, F., et al., 2009. Nili Fossae Data Processing Walkthrough. Presentation at CRISM Data Users Workshop. The Woodlands, TX
Seelos, K., et al., 2012. MTRDR Data Analysis Walk-through. Presentation at CRISM Data Users Workshop. The Woodlands, TX
Sefton-Nash, E., et al., 2015. The hypanis fluvial deltaic system in xanthe terra: a candidate exomars 2018 rover landing site. Proceedings of the Lunar and Planetary Science Abstract #1414.
Sharp, R.P., 1942. Mudflow levees. J. Geomorphol. 5, 222–227.
Shean, D.E., et al., 2016. An automated, open-source pipeline for mass production of digital elevation models (DEMs) from very-high-resolution commercial stereo satellite imagery. J. Photogram. Remote Sens. 116, 101–117.
Smith, D.E., et al., 2001. Mars orbiter laser altimeter: experiment summary after the first year of global mapping of mars. J. Geophys. Res.:Planets 106 (E10), 23689–23722.
Stanistreet, I.G., McCarthy, T.S., 1993. The okavango fan and the classification of subaerial fan systems. Sediment. Geol. 85, 115–133.
Stuurman, C., 2017. Ridges on martian debris-covered glaciers: deconvolving structural and climate processes. University of Texas at Austin M.sc thesis.
Summons, R.E., et al., 2011. Preservation of martian organic and environmental records: final report of the mars biosignature working group. Astrobiology 11 (2), 157–181.
Tanaka, K.L., 1997. Sedimentary history and mass flow structures of chryse and acidalia planitiae, mars. J. Geophys. Res.:Planets 102 (E2), 4131–4149.
Tanaka, K.L., et al., 2003. Resurfacing history of the northern plains of mars based on geologic mapping of mars global surveyor data. J. Geophys. Res. 108 (E4), 8043.
Tanaka, K.L., et al., 2014. Geologic map of mars. U.S. Geological Survey. Map 3292
Viviano-Beck, C.E., et al., 2014. Revised CRISM spectral parameters and summary products based on the currently detected mineral diversity on mars. J. Geophys. Res.:Planets 119 (6), 1403–1431.
Whalley, W.B., Azizi, F., 2003. Rock glaciers and protalus landforms: analogous forms and ice sources on earth and mars. J. Geophys. Res.:Planets 108 (E4), 8032.
Wood, L.J., 2006. Quantitative geomorphology of the mars eberswalde delta. GSA Bull. 118 (5–6), 557–566.